Surfaces and Interfaces 72 (2025) 107150

Contents lists available at ScienceDirect

Surfaces and Interfaces

journal homepage: www.sciencedirect.com/journal/surfaces-and-interfaces

An eco-friendly eugenol benzoxazine curcumin epoxy composites with modified nanocarbon fillers for enhanced corrosion protection

Malavalli Chidanandakumar Hithesh, Yadavanahalli Mahalingaiah Harsha, Kikkeri Narasimha Shetty Mohana *, Muralidharan Sreelakshmi, Mysore Chandru Sunil Kumar

Department of Studies in Chemistry, University of Mysore, Manasagangotri, Mysuru 570 006, Karnataka, India

ARTICLE INFO

Key words:
Barrier coating
Green nanocomposite
Bio-based polymer
Curcumin based epoxy
Mild steel

ABSTRACT

The current study demonstrates the development of an eco-friendly and sustainable anti-corrosion coating material derived from eugenol and curcumin. The eugenol benzoxazine-curcumin epoxy (EBCE) composite coating material was fabricated by blending the different ratios of EB and curcumin-based epoxy (CE) resin. Graphene oxide (GO) and multiwalled carbon nanotube (MWCNT) are amine functionalized with 5-amino-2,4-di-tert-butylphenol separately, and their effects on the anti-corrosion efficacy of EBCE was evaluated. The synthesized materials were characterized by FT-IR, XRD, Raman spectroscopy, XPS, EDX, FE-SEM, TGA, TEM, and SAED techniques. The surface morphology, hydrophobicity, and nature of the coatings were examined by AFM, contact angle (CA) measurements, and crosshatch adhesion test. The barrier performance of the coatings was ascertained using electrochemical impedance spectroscopy (EIS) and salt spray analysis (SSA). The EBCE (1:1) coating showed the CA of 77.47°, and coating and charge transfer resistances (R_c and R_{ct}) in the range of 10^5 Ω cm^2. Induction of 0.3 wt% functionalized multiwalled carbon nanotube (FMWCNT) into EBCE coating reliably enhanced the corrosion resistance property (R_c and $R_{ct} = 10^6$ Ω cm^2), and hydrophobicity (113.10°) up to 40^{th} day of immersion. Some of the reported coating formulations showed lesser R_{ct} ($\leq 10^5$ Ω cm^2) and hydrophobicity (<110°) compared to EBCE/FMWCNT (0.3 wt%) coatings. The higher surface area of FMWCNT core and compatibility with CE significantly enhanced the adhesion property of EBCE, and also densely occupy the voids in the coating matrix. Thus, EBCE (1:1) with 0.3 wt% FMWCNT demonstrated as a prospective material in anti-corrosion studies.

1. Introduction

The corrosion phenomenon is a major threat to metals, and their protection holds a key role in preventing damages to all the industrial sectors. Organic coating is a well-established technology for the active protection of metals from corrosion [1]. However, the present environmental protection society accentuating to replace the hazardous organic and petroleum-based materials with sustainable eco-friendly products due to their toxicity, health concerns to handlers, and disposal issues [2–4]. Some of the less toxic materials based on natural fatty acids and renewable plant sources [5,6], and sustainable benzoxazines coatings derived from plant oils are receiving attention in the field of corrosion protection [7,8].

The bio-based benzoxazine frontiers are swiftly expanding in the field of coating technology from past two decades [9–11]. The ease of flexibility in designing the benzoxazines from natural sources like cardanol, eugenol, vanillin, and catechol, make them an interesting material in many industrial, and coating applications like rocket nozzle protection [12], radiation shielding [13], aerospace composites [14], anti-corrosion coatings [15], and self-healing materials. Eugenol is a unique phenylpropanoid compound obtained from bio sources, and extracted from *syzygium aromaticum,* a native to Indonesia known as clove oil. It is generally used to treat toothache, skin disorders and inflammatory conditions, and known to fight against oral bacterium [16,17]. Eugenol based benzoxazines act as natural defenders against the corrosion phenomenon due to their thermal resistance, high crosslinking ability, and hydrophobicity [18,19]. Solely employing benzoxazines in corrosion prevention strategies can result in brittle coatings, demanding

* Corresponding author: Ph: +91 94496 27573
E-mail address: drknmohana@gmail.com (K.N.S. Mohana).

https://doi.org/10.1016/j.surfin.2025.107150
Received 12 May 2025; Received in revised form 26 June 2025; Accepted 6 July 2025
Available online 8 July 2025

higher curing temperature, and slow curing processes. Hence, composite preparations involving benzoxazines with epoxy resins, and nanofillers refine toughness, water repellence, and less curing temperature of coating formulations [20,21]. Conventional epoxy resins are prone to develop pores, cracks, and their complete dependency on the filler materials to enhance their anti-corrosion properties makes them an issue to be looked upon [22–26]. In view of this, non-hazardous, and eco-friendly epoxy resin derivatives need to be developed in the anti-corrosion coating studies. Curcumin is one such non-toxic polyphenolic compound majorly found in turmeric, shows potential anti-oxidant and anti-inflammatory properties. Eco-friendly, hydrophobic and recyclable nature of curcumin prompted to employ it in anti-corrosion investigations by subjecting it to simple one-step epoxidation. The epoxies derived from curcumin are thermosetting bio-based resins, and are known to act as prominent corrosion inhibitors [27,28]. Curcumin assists in enhancing the crosslinking, chain extension, and increases the probability of hydrogen bonding with the polymer matrix [29]. With above properties, epoxy resins derived from curcumin is a budding candidate to be employed as anti-corrosion coatings.

Benzoxazine derived from eugenol forms bio-based polybenzoxazine easily without additional polymerizing catalysts. The eco-friendly nature, hardness and low flammability make it suitable for industrial usages. Its ability to undergo functionalization assists in the dispersion of nanofillers, and adhesion of the coatings due to the presence of aromatic groups. The eugenol benzoxazine is naturally hydrophobic, further its hydrophobicity increases on curing by forming dense crosslinked network and denying the entry to corrosive agents [30]. On the other, curcumin-based epoxies are non-toxic, safer even when contacted on skin, possess high chemical resistance in comparison with conventional epoxy resins, and aids in uniform distribution of nanomaterials due to the presence of polar group in its core structure. The chelation properties of the curcumin diminish the corrosion sites with higher adsorption affinity to metals [31]. Recently eucalyptus oil-based polyurethane (PU) coating was developed by Nogueira *et al.,* and the results showed improved thermal stability, adhesion and anti-corrosion performance compared to traditional petroleum-based coatings [32]. Bio-based water borne polyester modified with cellulose nanofiber and rGO/ZnO nanocomposite was prepared, and their corrosion inhibition studies showed excellent anti-corrosion efficacy [33]. The sesamol based benzoxazine acts as an efficient thermoset, and the presence of aromatic oxazine group contributes to the enhanced mechanical properties, and hydrophobicity [34]. The adhesion and hydrophobic performance of benzoxazine based materials can be further enhanced by the addition of fillers, and resinous copolymeric materials, promoting its applicability in the coating technology. The silicon/eugenol-based derivative was reported as an efficient anti-corrosion coating material [35]. The thermal property of eugenol based benzoxazine polymer was reported by Thirukumaran *et al.* [36]. The mixed benzoxazine precursors synthesized from eugenol and phenol showed high thermal stability with enhanced crosslinking [37]. Eugenol-pyrogallol copolymer benzoxazine coatings showed superior corrosion protection in saline medium up to 30 days of immersion [38]. Eugenol benzoxazine fabricated with bio silica and natural fibrous materials were studied for crosslinking ability, and corrosion resistance [39,40]. Contemporarily, bio-based polymers act as sustainable and eco-friendly alternative coating materials compared to petroleum-based coating systems [41,42]. In view of the outstanding characteristic assets of eugenol and curcumin combination made us to explore their synergy in the anti-corrosion studies.

Graphene based nano fillers are employed in material applications due to their exceptional strength, improved mechanical, thermal stability and corrosion barrier properties [43]. They are proven to be efficient reinforcement filler materials in the field of corrosion studies to uplift the coating materials performance [44,45]. Both GO and MWCNT belong to carbon-based nanomaterials, nonetheless their structural features, mechanism of protection, compatibility, optimization role, and dispersion in the coating matrix varies significantly [46,47]. Mixing GO and MWCNT into a single matrix might reduce the optimal performances due to their incompatible geometries (2D and 1D), dissimilar surface chemistry which can lead to uneven dispersion, phase separation, and agglomeration in the matrix. Also, GO could wrap around the tube-like structures of MWCNT affecting their individual performances [48]. The bio-based matrix interaction with GO and MWCNT individually can affect in water interaction phenomenon, and creating a discrepancy in the hydrophobic nature of the coating. MWCNT incorporated coatings possess high interfacial area between the coating matrices and offer excruciating path for ionic movement due to is fine distribution, increasing the barrier performance of the coatings [49]. Chemical functionalization like amidation, esterification, silanization and polymer grafting plays a crucial role in tuning the pristine filler material properties. The addition of minuscule amount of functionalized nano fillers into the composite materials improves the adhesion, hardness, and corrosion resistance [50]. Jing *et al.* synthesized a silanized GO, and evaluated its anti-corrosion performance [51]. The anti-corrosion performance of PU coating was improved by the incorporation of covalent functionalized GO [52]. Polyamido-amine dendrimer functionalized GO incorporated epoxy coating demonstrated a dependable corrosion resistance [53]. 2-Amino-4,6-dichloropyrimidine modified GO blended fluorinated polyurethane coating enhanced the corrosion protection ability of the coating matrix [54].

All the above grounds for contracting the two carbon-based filler materials individually into EBCE for the prevention of mild steel (MS) corrosion. In the present work an eco-friendly, sustainable, and original composite material derived from eugenol based benzoxazine and epoxidized curcumin was developed. The eugenol benzoxazine (EB) was synthesized by mannich type reaction, and curcumin epoxy (CE) resin was synthesised using curcumin. They are blended to form a EBCE composite material, and assessed its anti-corrosion performance. Further, the GO and MWCNT were modified with 5-amino-2,4-di-tert-butylphenol, and the anti-corrosion evaluation of EBCE with different wt% of FGO and FMWCNT was also explored.

2. Experimental

2.1. Materials

Eugenol, 1–hydroxybenzotriazole (HOBt), 1–ethyl–3–(3–dimethylaminopropyl) carbodiimide (EDCI) were purchased from Avra synthesis pvt. Ltd., multiwalled carbon nanotubes obtained from ultrananotech Ltd., graphite flakes, potassium permanganate, concentrated hydrochloric acid, concentrated sulphuric acid (98%), sodium nitrate, 30% hydrogen peroxide solution, triethyl amine, formaldehyde, sodium hydroxide pellets, aniline, anhydrous sodium sulphate, and glacial acetic acid were obtained from S.D. Fine Chem Ltd., 5-amino-2,4-di-tert-butylphenol (DTB) was purchased from Sigma Aldrich Ltd. Emery papers of grades 1/0, 2/0, 3/0, 4/0, 5/0, 6/0, 7/0 were used to smoothen the surface of MS. The MS specimen with the composition of S (0.012%), Mn (0.13%), C (0.05%), Si (0.05%), P (0.010%), Al (0.1%) and Fe (99.6%) was used in the anti-corrosion studies.

2.2. Methods and characterization techniques

Perkin Elmer FT-IR spectrophotometer was used to confirm the functionalization of the nano fillers in the spectral range of 500-4000 cm^{-1}. Rigaku D/max2200PC diffractometer equipped with sealed 2kW X-ray tube utilizing CuKα radiation, and a scan rate of 0.1/6 (°/min) in the reflection mode was used for the P-XRD investigations. Xplore plus Raman microscope of Horiba Scientific was used to acquire the Raman spectra of FGO and FMWCNT. The X-ray photoelectron spectra were obtained with the model PHI 5000 Versa Probe II, FEI Inc, operated in a rotating anode with 100W high power, in a highly sensitive non-dispersive monochromator X-ray beam, and adjustable rectangular area from 0.1 to 0.5 mm. The surface roughness parameters of the coated

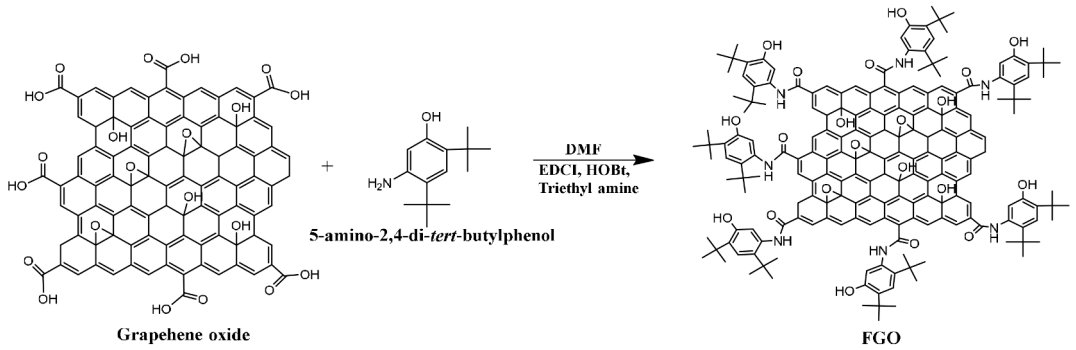

Scheme 1.1. Functionalization of graphene oxide.

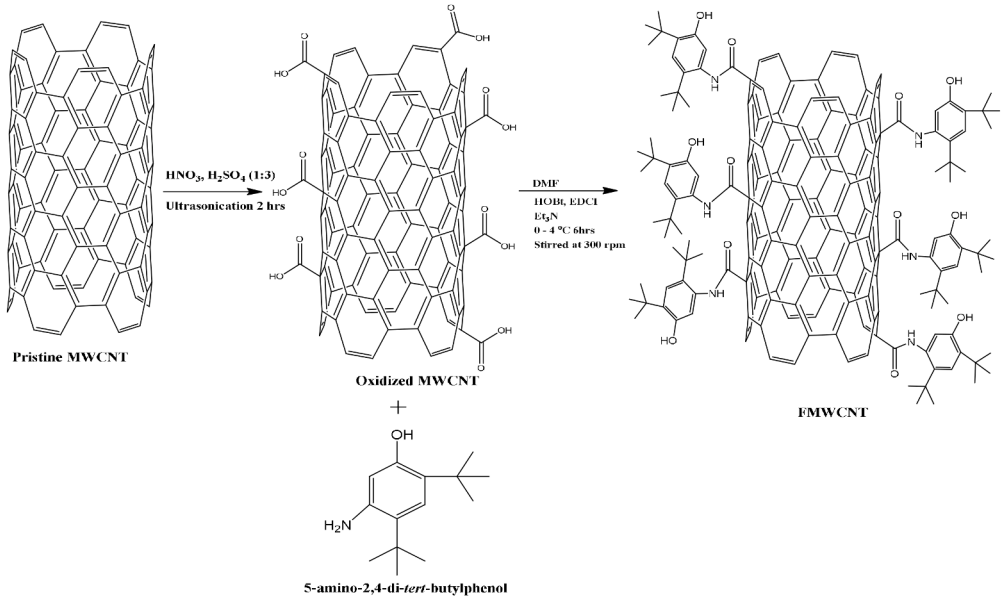

Scheme 1.2. Functionalization of MWCNT.

samples were analysed by SPM atomic force microscope of the make Innova, equipped up to 100 μm scanner in a tapping mode. The surface morphologies of FGO and FMWCNT were obtained with FE-SEM Ultra plus, Carl Zeiss. The thermal stability FGO and FMWCNT was evaluated by TA instruments, SDT Q600 model equipped with dual beam horizontal balance and furnace. The TEM images were obtained by G2-20 TWIN FEG with the quantum SE 963 fitted, 2k x 2k CCD camera operated at 200 kV, super twin lens featured with Gatan imaging filter, and filtered diffraction patterns of the make FEI – TECNAI. The contact angle measurements were done using the sessile drop method with deionised water at room temperature of Kyowa DMs-401. The electrochemical workstation, CHI608E, USA, was used to study the anti-corrosion performance of the coated samples. Priorly, the mild steel (MS) samples were cut into 2 × 5 cm (width × length). The desired dimensions of MS coupons were immersed in dilute HCl solution for 10 minutes to remove the pretreated zinc coatings. Afterwards, it was thoroughly washed with distilled water and dried completely. The dried MS specimens were smoothened with different grades of emery sheets (1/0 to 7/0), and washed with distilled water followed by ethanol, and acetone, finally dried before coating. The salt spray analysis was carried out at 35 °C chamber temperature and pH of 6.8 by ASTM B117-19 method.

2.2.1. *Functionalization of graphene oxide*

The GO was synthesized by following the modified hummer's method. In a clean dry round bottom (RB) flask, 400 mg of the synthesized GO was dispersed in 99.9 % ethanol in a ultrasonicator for 45 mins and transferred the RB flask to magnetic stirrer, and maintained at 0 - 4 °C in an ice bath. Then, the coupling agents, HOBt (0.488 g, 0.00361 moles), EDCl (0.692 g, 0.003614 moles), and 2 ml of triethylamine were added. Then, 400 mg (0.001807 moles) of 5-amino-2,4-di-tert-butylphenol (DTB) dissolved in minimum amount of N, N-dimethyl formamide was immediately added into the reaction mixture and stirred for 6 hours at 0 - 4 °C. Later, the temperature was raised to 80 °C and continued stirring for overnight. After the completion of the reaction, the contents were ultrasonicated for 5 mins, followed by percolation of the obtained FGO, and washed with distilled water and ethanol several times, finally, dried in a hot air oven at 70 °C for 90 mins. Its synthetic route is presented in Scheme 1.1.

2.2.2. *Functionalization of multi-walled carbon nanotubes*

The functionalization of MWCNT was carried out in 2 steps (Scheme 1.2). Initially, 500 mg of pristine MWCNT was added into a 1:3 acid mixture of HNO_3 and H_2SO_4 to introduce oxygen containing functionalities. The above contents were ultrasonicated for 1 hr at 45 °C to attain a fine dispersion of the particles, and then stirred at 90 °C for 6 hrs on a magnetic stirrer. After the completion of reaction, the contents were neutralized with double distilled water, rinsed and centrifuged with 99.9% ethanol to get the oxidized MWCNT (OMWCNT). The obtained product was dried at 70 °C for 5 hrs in a hot air oven.

The oxidized MWCNT (300 mg) was dispersed in 5 ml ethanol taken

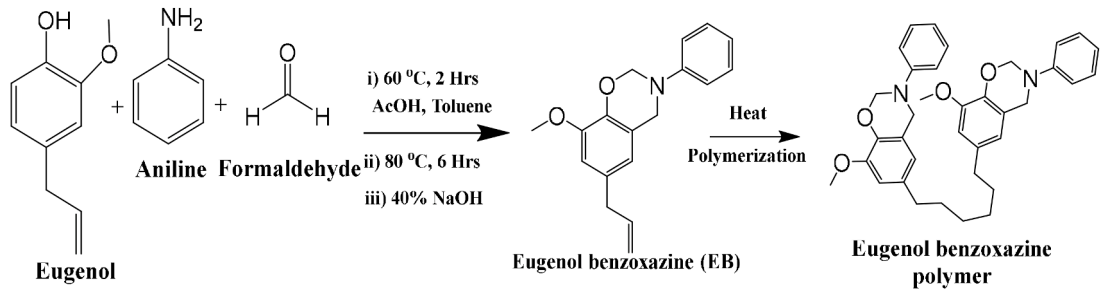

Scheme 1.3. Route for the synthesis of eugenol benzoxazine.

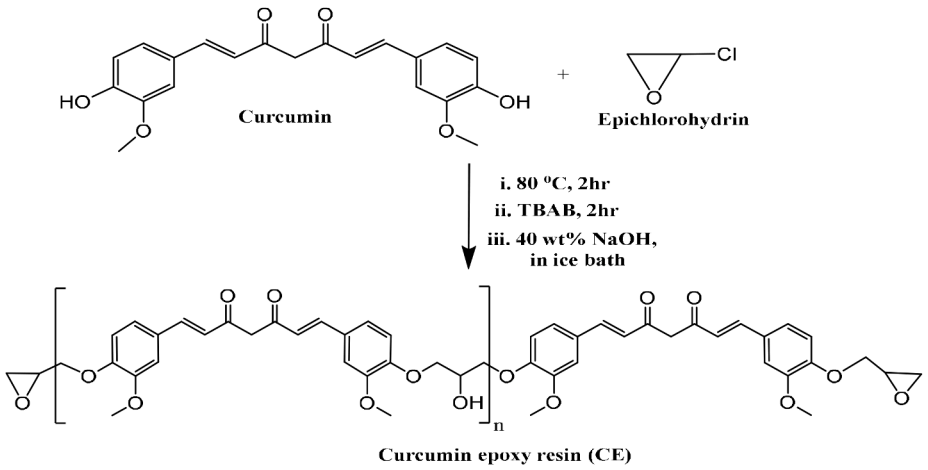

Scheme 1.4. Route for the synthesis of curcumin epoxy resin.

in a clean dry 100 ml RB flask and ultrasonicated for 1 hr with a 30 min interval. The RB flask was transferred to magnetic stirrer (300 rpm) and maintained at 0 – 4 °C in an ice bath. Subsequently, the coupling agents HOBt (0.6103 g, 0.004517 moles) and EDCI (0.8659 g, 0.004517 moles) were added. Then, 400 mg of 5-amino-2,4-di-tert-butylphenol priorly dissolved in 8 ml of ethanol and 1.5 ml of triethyl amine was successively supplemented. The above reaction mixture was stirred at 0 – 4 °C for 5 hrs in an ice bath, and continued stirring by maintaining room temperature for 12 hrs at 700 rpm. Once the reaction is completed, the contents were ultrasonicated for 5 mins, washed with de-mineralized water, tailed by ethanol to remove the impurities to get black powder. The obtained product was dried for 5 hrs at 78 °C in a hot air oven and labelled as FMWCNT.

2.2.3. *Synthesis of eugenol based benzoxazine*

Eugenol based benzoxazine was synthesized by following the literature method [55]. Briefly, in a dry 2 necked RB flask, 7.5 ml of eugenol was dissolved in toluene and 3.7 ml of formaldehyde was added, and then stirred at 60 °C for 2 hrs, followed by the addition of 4.5 ml of amine source, and the contents were vigorously stirred at 80 °C for 12 hrs. Then, 2N NaOH solution was slowly added until the yellow brownish product of eugenol based benzoxazine was formed. The

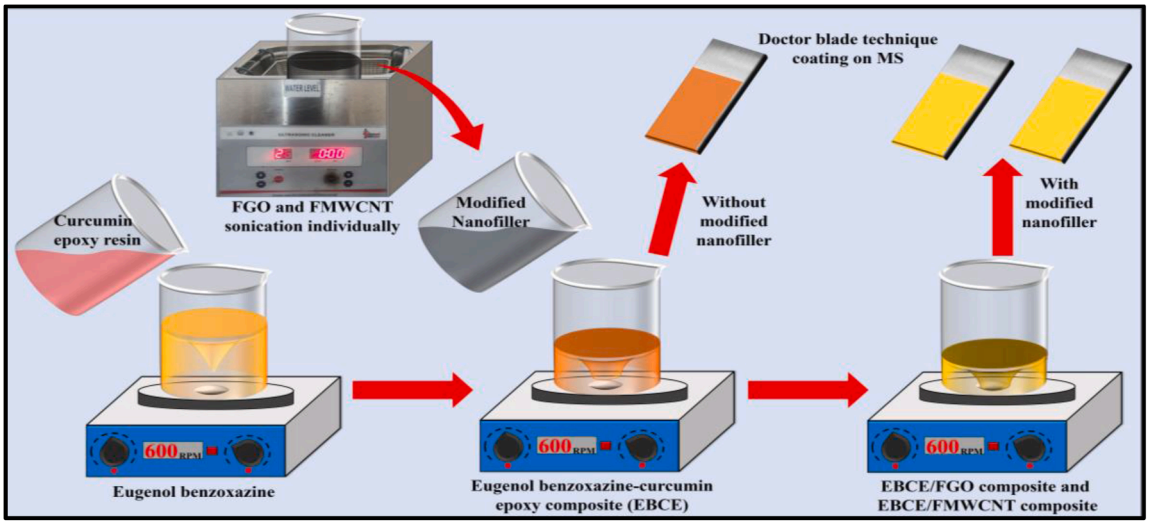

Scheme 1.5. Schematic route for the synthesis of EBCE, EBCE/FGO, and EBCE/FMWCNT coatings.

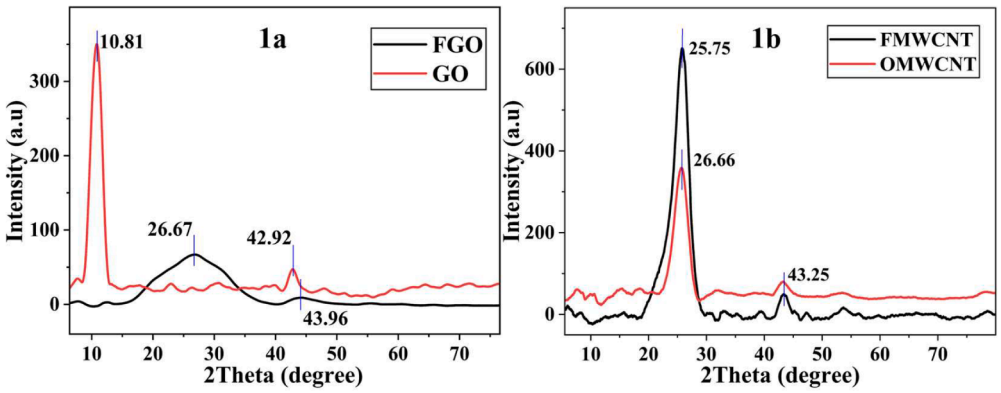

Fig. 1. XRD patterns of (a) GO, FGO and (b) OMWCNT, FMWCNT.

obtained product was washed and separated using chloroform. The synthesized eugenol benzoxazine (EB) was stored in a desiccator. The synthetic route is given Scheme 1.3.

2.2.4. Synthesis of curcumin-based epoxy resin

Curcumin epoxy (CE) resin was synthesized by stirring curcumin (1 g) and epichlorohydrin (4.5 ml) at 80 °C on a magnetic stirrer for 2 hrs. Tertiary butyl ammonium bromide (0.525 g) was added as the catalyst to the above mixture and continued stirring for 2 hrs. The reaction mixture was allowed to cool and transferred to ice bath. Then, 40% NaOH solution was gradually added to the above reaction mixture to get a brown precipitate of the CE resin, which was further stirred for 6 hrs in ice-cold condition. The obtained product was extracted with ethyl acetate and washed with brine solution, trailed by the removal of any water content using anhydrous sodium sulphate from the organic layer. Finally, the product was stored in a desiccator. The synthetic outline is presented in Scheme 1.4.

2.2.5. Fabrication of eugenol benzoxazine-curcumin epoxy, EBCE/FGO and EBCE/FMWCNT coatings

Initially, 0.3 g of EB and 0.3 g CE resin (1:1) are taken in two different clean beakers and dissolved in 5 - 7 ml of chloroform. The EB solution was stirred at 80 °C for an hour. Then, the prepared CE resin solution was gradually added to the EB solution and continued stirring at 600 rpm for 3 hrs. The appearance of brownish orange color solution indicates the formation of EBCE. The composite solution was stirred further to get the gluey appearance till the occurrence of coating consistency by ensuing slow solvent evaporation technique to obtain the coating composite (Scheme 1.5). Similar procedure was followed by taking appropriate quantities of EB and CE in the preparation of 1:2 and 2:1 EBCE. The obtained coating materials are coated on the MS surface using doctor blade technique in 2 sets, and 2 trails were performed for each set. All the MS coated samples were cured at room temperature for 48 hrs to prevent crack formation, followed by curing in hot air oven from 50 °C up to 140 °C with the increment of 30 °C, and the thickness of the single layer of the applied coating was found to be 36 μm.

3. Result and discussion

3.1. X-ray diffraction studies

Fig. 1(a-b) represents the XRD patterns of pristine GO, FGO, OMWCNT, and FMWCNT. The extent of amine functionalization and changes in the crystallinity were estimated using the nature and intensity of the peaks along with the 2θ values. The definite sharp peak of GO (10.81° with 001 plane) was disappeared after the chemical modification by transforming into a broad peak at 26.67° (002 plane) in FGO, indicating the deviations occurred on the highly ordered arrangements of GO sheets, and unveiling the amorphous nature of FGO. The satellite peaks at 42.92° (100 plane) and 43.96° (100 plane) insisting graphitic defects induced due to the interaction of coupling agents and DBT with the GO. In addition, the d-spacing was decreased from 8.17 Å (GO) to 3.33 Å (FGO) indicating the integration of DBT onto the GO skeletal core and exfoliation of its sheets by noting a clear difference in the d-spacing values [56]. The OMWCNT exhibited the 2θ value of 25.27° with 3.45 Å d-spacing. After the chemical modification, similar peak was noticed (2θ = 26.66°, 002 plane), which could be due to retention of unbroken graphitic core and intact inner cylindrical structure of MWCNT [57]. The crystallite size (D) of the particles was determined by Scherrer equation (Eq. 1) using full width half maximum (FWHM) values from the obtained XRD peaks. The D of FGO (1.25 nm) and FMWCNT (3.48 nm) were reduced compared to their respective pristine GO (2.74 nm)

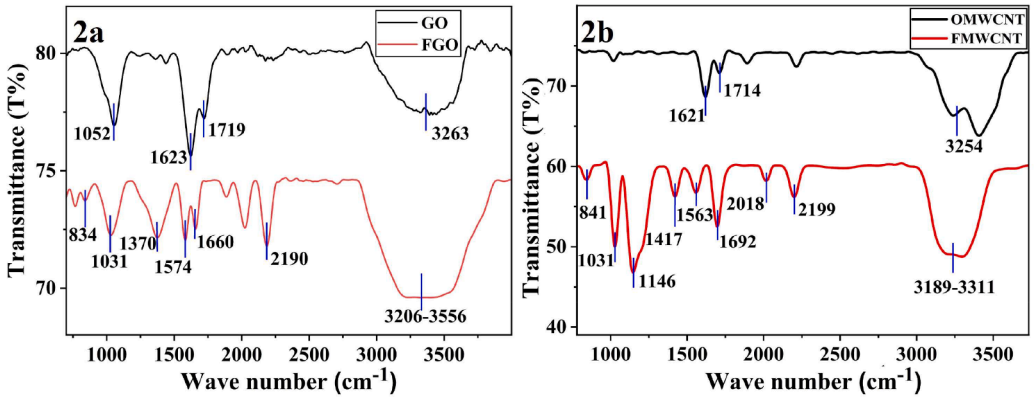

Fig. 2. FT-IR spectra of (a) GO, FGO and (b) OMWCNT, FMWCNT.

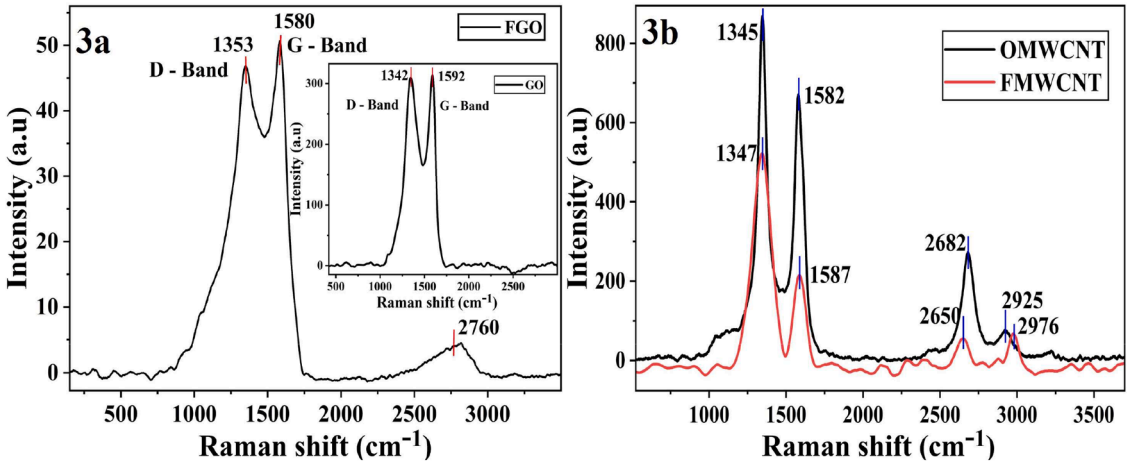

Fig. 3. Raman spectra of (a) GO, FGO and (b) OMWCNT, FMWCNT.

and OMWCNT (3.43 nm), indicating the decrease in the size of nano-fillers after functionalization [57,58].

$$D = \frac{k\lambda}{\beta \cos\theta} \quad (1)$$

3.2. FT-IR spectral studies

The FGO and FMWCNT were compared with GO and OMWCNT by FT-IR spectral analysis (Fig. 2). The presence of epoxy group (C-O-C) was confirmed by a band at 1052 cm^{-1}, and the sp^2 graphitic core (C=C) of GO and OMWCNT was found in the range of 1620 – 1624 cm^{-1}. The stretching modes of carboxylic acid and hydroxyl groups (-OH) of GO and OMWCNT are seen at 1719 cm^{-1}, 1714 cm^{-1} and 3263 cm^{-1}, 3254 cm^{-1} respectively, indicating complete oxidation of graphite flakes and MWCNT [59]. The appearance of absorption peaks at 1660 cm^{-1} and 1692 cm^{-1} for FGO and FMWCNT, respectively confirms the formation of amide group [(C=O)-NH] [60]. Correspondingly, the bands at 1574 cm^{-1} and 1563 cm^{-1} designates the N-H bending of amide moiety in FGO and FMWCNT [61]. Further, the desertion of carboxylic acid peak re-assures the successful amide functionalization. The C-H bending vibrations of benzene molecule are noticed at 831 cm^{-1} and 841 cm^{-1} [62].

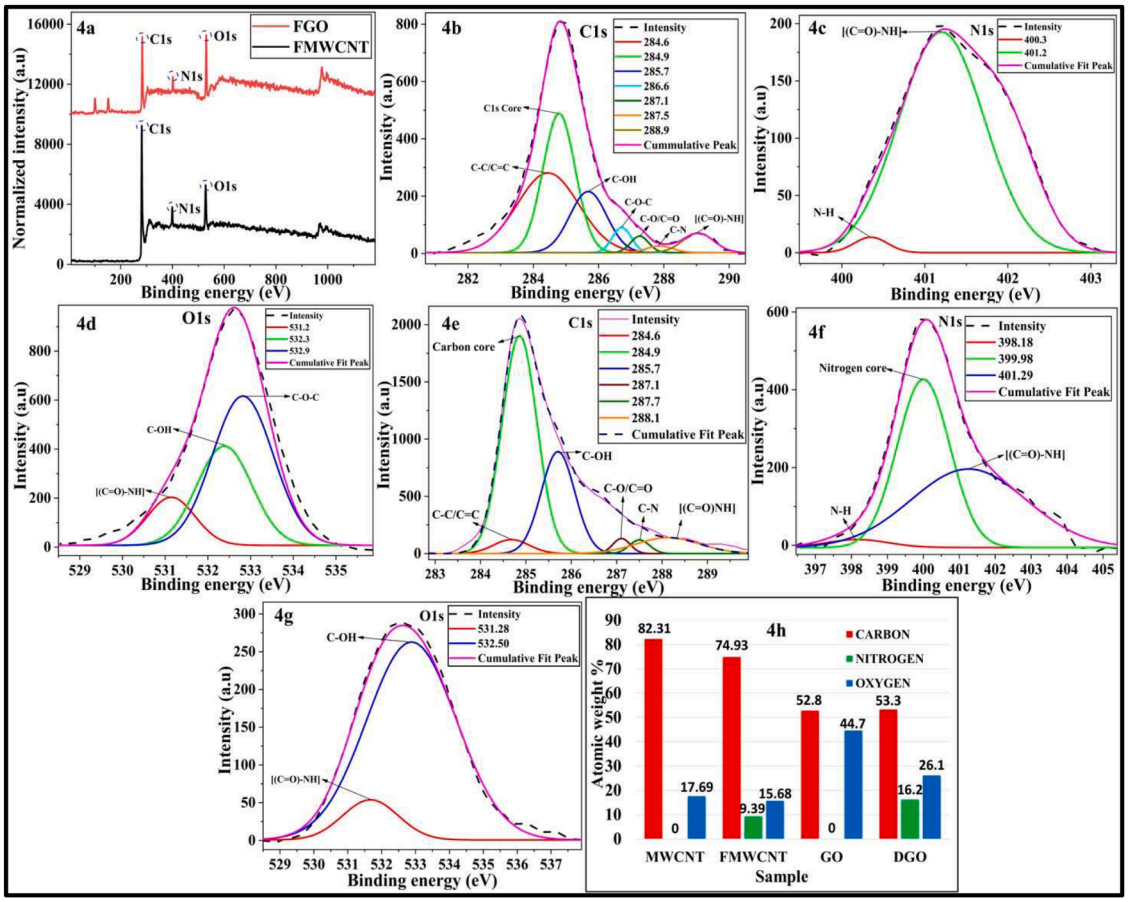

Fig. 4. XPS survey of (a) FMWCNT, and FGO, Simplified (b) C1s, (c) N1s, (d) O1s of FGO, (e) C1s, (f) N1s, (g) O1s of FMWCNT, (h) EDS of FMWCNT and FGO.

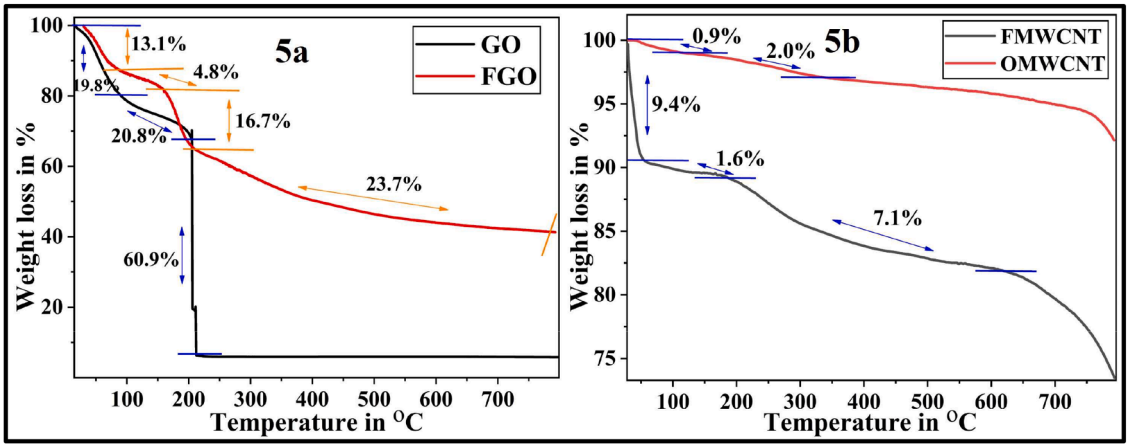

Fig. 5. Thermograms of (a) FGO and (b) FMWCNT.

The -OH absorption bands obtained in the range of 3180 cm^{-1} – 3560 cm^{-1} for FGO and FMWCNT.

3.3. Raman studies of FGO and FMWCNT

The Raman spectral plots of GO, OMWCNT, FGO and FMWCNT are depicted in Fig. 3. The peak intensities, D and G bands were used to identify the structural changes occurred in the hexagonal core, and hybridization of the existing carbon atoms in the nanofiller core. The high intense D-band with a value of 1342 cm^{-1} and G-band with 1592 cm^{-1} for GO are recognized, while the FGO displayed a shift in their values to 1353 cm^{-1} and 1580 cm^{-1} for D and G bands, respectively with decreased intensity. This suggests the intercalation of DBT molecule with GO. Additionally, the intensity ratios (I_D/I_G) of GO (0.927) and FGO (1.096) showed a definite upsurge after amine functionalization [63]. The D and G bands of FMWCNT were seen at 1347 cm^{-1} and 1587 cm^{-1}, respectively. This clearly indicates the shift in the band values compared to OMWCNT (D-band = 1345 cm^{-1}, G band = 1582 cm^{-1}) as seen in the Fig. 3b. The larger difference in the intensities of D and G bands in case of FMWCNT confirms the change in the hybridization from sp^2 carbon to sp^3 carbon due to the formation of amide moiety. The 2D bands noticed in the range of 2650 - 2980 cm^{-1} are the overtone peaks which designate the oxidation followed by amine functionalization. Furthermore, the higher I_D/I_G ratio quotes for the modification of side walls of the filler material, where FMWCNT (1.490) exhibited increased I_D/I_G ratio compared to OMWCNT (1.297) [64–67].

3.4. X-ray photoelectron spectroscopy and EDX spectral studies

The elemental composition and functional groups of modified nanofillers are probed by X-ray photoelectron spectroscopy (XPS), and are represented in Fig. 4. The presence of core elements *viz.,* carbon, oxygen, and nitrogen are depicted in Fig. 4a, signifying the addition of DBT molecule on to the surfaces of GO and OMWCNT. The graphitic core for C1s peak was seen at 284.9 eV in both FGO and FMWCNT (Fig. 4b and 4e). The sp^2 C-C/C=C of skeletal graphene structure and the oxidized functional groups such as C-OH and C-O/C=O were attributed to the presence of peaks at 284.6 eV, 285.7 eV, and 287.1 eV for both FGO and FMWCNT. The amine functionalization can be ascertained by the presence of peaks corresponding to C-N group of amide in the range of 287.5 - 287.7 eV, and carbonyl group of amide in the range of 288.1 - 288.9 eV [68]. The N1s simplified plots depicted in Fig. 4c and 4f interpret the nitrogen bound to carbonyl group at 401.2 eV. These confirm the covalent amine functionalization by the formation of amide and N-H bonds, and are assigned to 400.3 eV and 398.1 eV for FGO and FMWCNT, respectively [69]. Supplementing the above, the existence of

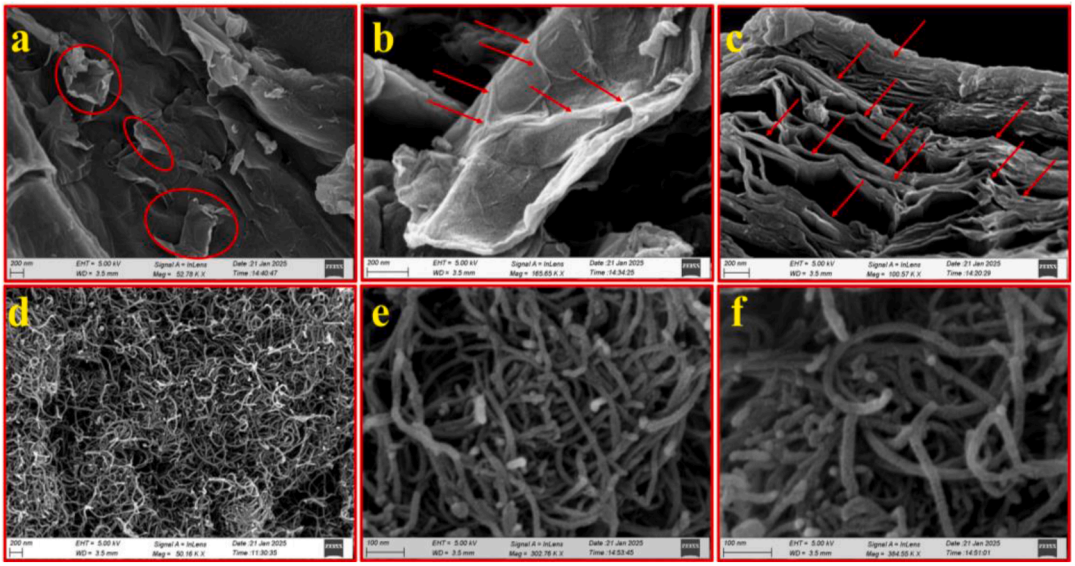

Fig. 6. FE-SEM images of (a-c) FGO, (d-f) FMWCNT.

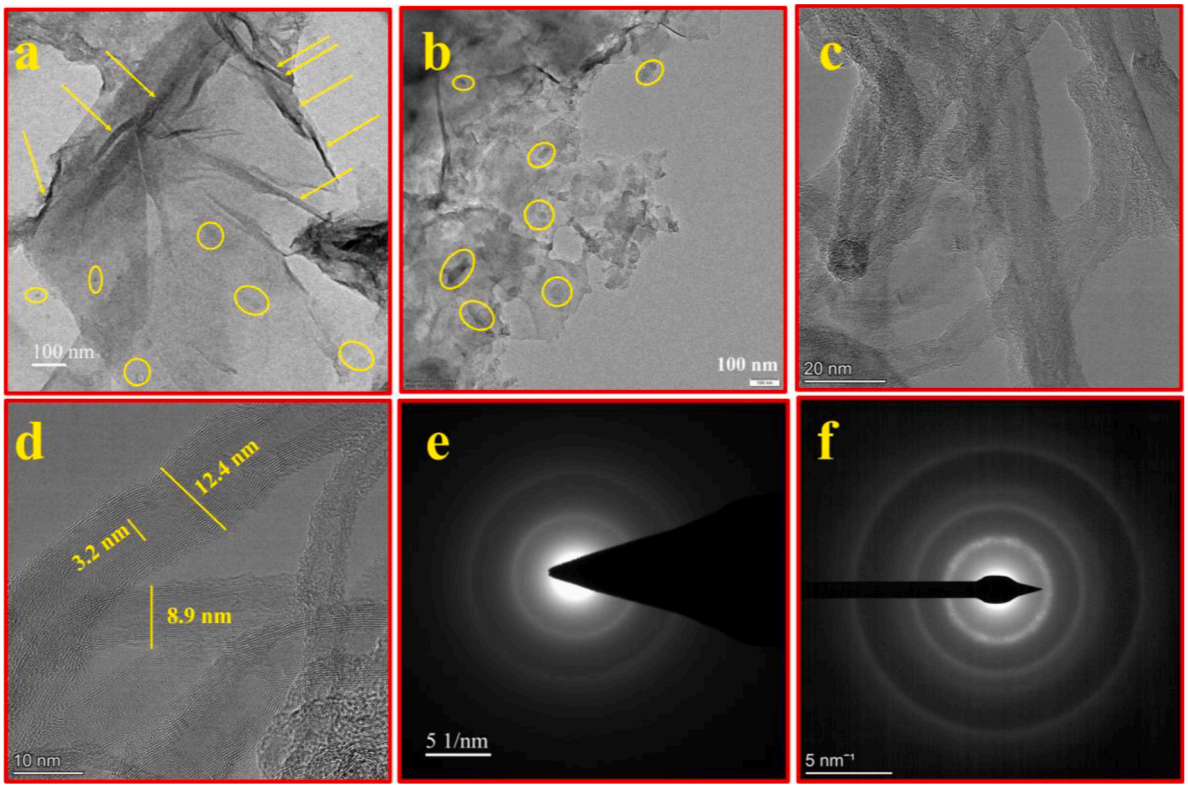

Fig. 7. TEM images of (a-b) FGO, (c-d) FMWCNT, and SAED patterns of (e) FGO and (f) FMWCNT.

-[(C=O)NH] and C-OH groups positioned at 531.8 eV and, between 532.3 eV and 532.5 eV are recapitulated in O1s plots (Fig. 4d and 4g) [70]. The EDS data summarized in Fig. 4h shows the presence of 52.6% and 82.3% of carbon in GO and MWCNT, respectively. The presence of 44.7% and 17.7% of oxygen content depicting the complete oxidation of GO compared to MWCNT. Further, FGO and FMWCNT contain 16.1% and 9.3% of nitrogen, 53.3% and 74.9% of carbon and 26.1% and 74.9% oxygen, respectively.: The degree of functionalization (DOF) of nitrogen was estimated with N/C ratio using Eq. 2. The atomic percentages of nitrogen content in the functionalized nanofillers are directly related higher degree of functionalization. The DOF of N content in FGO and FMWCNT are found to be 5.14 and 12.2. The atomic percentages are presented in Table S6 of the supplementary section.

$$DOF = \frac{N}{C} \times 100 \quad (2)$$

3.5. Thermogravimetric analysis of FGO and FMWCNT

The thermograms of the synthesized materials are obtained by plotting weight loss in percentage as a function of change in temperature in the N_2 atmosphere (Fig. 5). Initially, pristine GO lost 19.8% and FGO lost 13.1% of their respective mass in the form of volatile and moisture content in the range of 60 - 90 °C. The second stage of GO decomposition occurred from 100 - 230 °C with the loss of 20.8% due to the removal of oxygenated functionalities, while the major mass loss (60.9%) of carbon hexagonal core was seen above 220 °C. The FGO displayed a minimal loss of 4.8% in the secondary decomposition phase, then perceived 16.7% of weight loss in later stages due to the breakdown of DBT molecule followed by delayed consistent weight loss (23.7%) up to 800 °C indicating that FGO displayed thermally more stable compared to pristine GO [71]. The OMWCNT revealed the weight loss of 0.9% and 2% indicating the loss of oxygen functionalities. Beyond this point it is stable with the detection of insignificant amount of weight loss in the range of 100 – 750 °C due to amorphous nature of carbon in the core structure of MWCNT [72]. In case of FMWCNT, the removal of volatile components took place up to 70 °C (9.4% mass loss), and resistance to thermal degradation was witnessed till 230 °C with the narrow loss of 1.6% of its mass indicating the loss of few oxygenated species. From 230 - 710 °C, the secondary tedious mass loss was noted (Fig. 5b) due to the successful integration of DBT molecule into MWCNT, indicating the bonding integrity of the FMWCNT. Above 710 °C a steep fall initiates, pointing at the loss of all functional groups leaving only carbon core of MWCNT.

3.6. Field emission-scanning electron microscopy of FGO and FMWCNT

Fig. 6 elucidates the FE-SEM images of FGO and FMWCNT. The morphology of FGO shows the defect induced layers on the surface of graphene sheet. The shiny edges are due to the alterations of GO sheets occurred during the course of interaction between the coupling agents and the GO sheet (Fig. 6a-b). The disorganized arrangements of the stacked graphene skeletal sheets (Fig. 6c) validate the decreased intensity and broadening of the peaks observed in XRD. The Fig. 6d shows fine distribution of CNTs, and the tubular surface structure possessed a coarse nature with edges and glittering like deposition on few regions of the sides of CNTs walls. The above reasons for the interaction of 5-amino-2,4-di-tert-butylphenol with GO and MWCNT.

3.7. Transmission electron microscopy and SAED patterns of FGO and FMWCNT

TEM images of FGO and FMWCNT are depicted in Fig. 7. FGO visibly shows exfoliated wrinkled like graphene sheets and the dark spots on its surface could be due to the intercalation of the DTB with GO via amide bond (Fig. 7a-b). FMWCNT possess the fine tubular structure with visible ends, and the outer walls of the CNTs have rough nature, which could be occurred on the course of modification reaction. The multiple layers of the inner walls of nanotube are presented in the magnification range of

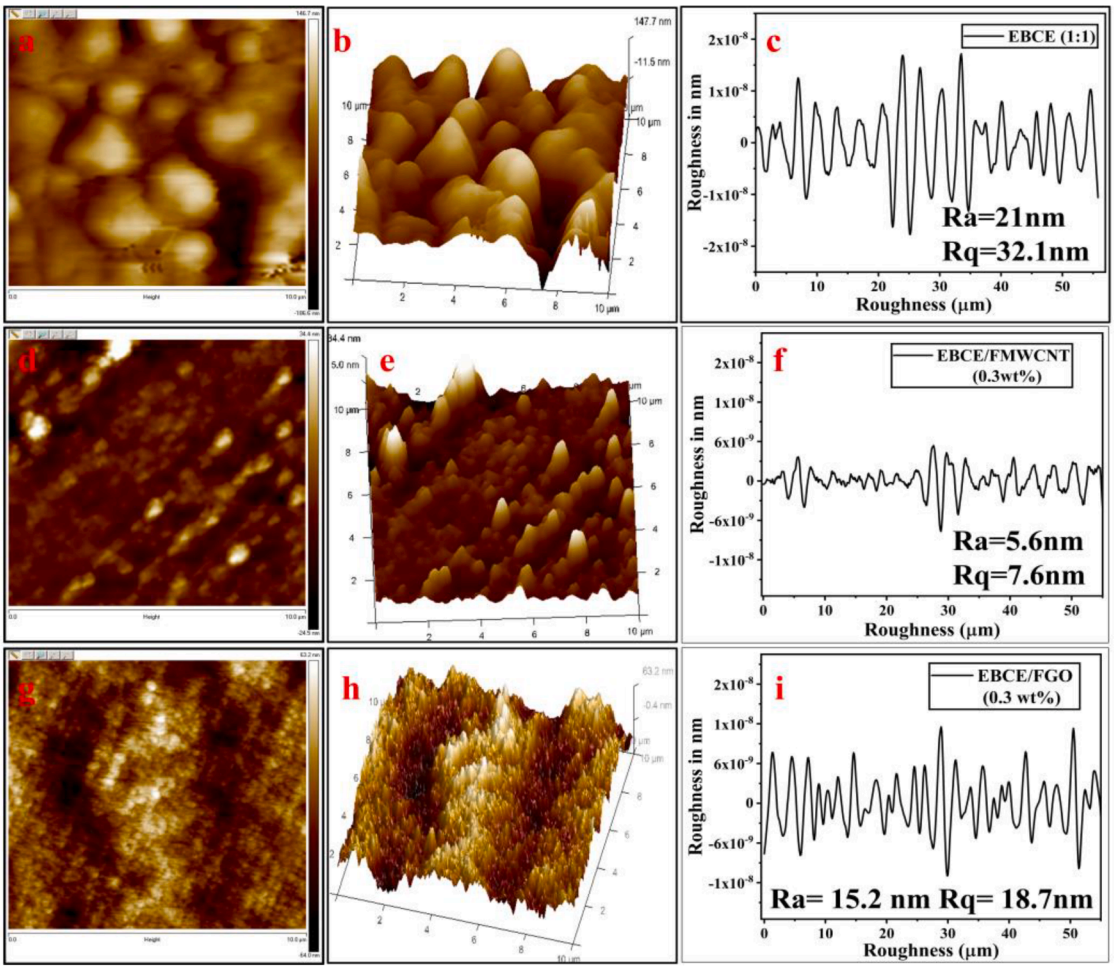

Fig. 8. 2D, 3D topographical images and roughness graphs of (a-c) EBCE (1:1), (d-f) EBCE/FMWCNT (0.3 wt%), and (g-i) EBCE/FGO (0.3 wt%) coated MS samples.

20 nm and 10 nm (Fig. 7 c & d). MWCNT has the size of 12.4 nm with 8.9 nm outer diameter and 3.2 nm of inner diameter as seen in the Fig. 7d. In addition, the SAED patterns of FGO and FMWCNT are presented in Fig. 7 (e-f). The nature of the diffraction rings shows the diffusing ring form, indicating their amorphous nature after chemical modification. Further, the diameters of the diffraction rings were used to acquire the d-spacing of 3.68 Å and 3.41 Å for FGO and FMWCNT, respectively, which were found to be in agreement with XRD studies.

3.8. Atomic force microscopy and contact angle measurements of coated samples

The quantitative and qualitative statistics of the coatings were evaluated using AFM at 10 × 10 μm scan rate in a tapping method. The alteration in EBCE (1:1) coating with and without the incorporation of different nanofillers was reported. Fig. 8 (a-b) and 8 (g-h) depicting the clean EBCE (1:1) and EBCE/FGO (0.3 wt%) coatings which exhibit more hills and gorges, and their coating surfaces showed 21 nm, 32.1 nm and 15.2 nm, 18.7 nm of average roughness (R_a) and root mean square roughness (R_q), respectively. Higher roughness could contribute to electrochemical corrosion affecting the barrier performances of the coatings, by facilitating increased active surface area to interact with corrosive species which in turn enable easier mass transport across coatings and substrate resulting in least charge transfer resistance and increase the capacitance of the coatings [73]. Further, more waviness of the profile, easily causes the coating to disintegrate, and initiate the corrosion process by creating the clogging site, Induction of 0.3 wt% FMWCNT into the EBCE reduces the roughness, and its R_a and R_q values were found to be 5.6 nm and 7.6 nm. Its 2D image shows reduced pits, defects, and smoother coating surface. Additionally, lesser profile height was seen in its 3D image compared to other samples. The gaps in the coating are filled by the nanofiller which help to achieve denser packing of the inter-molecular bonding, thereby enhancing the hydrophobicity and hence the anti-corrosion performance.

The hydrophobic nature of the EBCE (2:1), EBCE (1:1), EBCE (1:2), and different wt% of FGO and FMWCNT incorporated EBCE coated MS samples are estimated by measuring contact angle (CA) (Fig. 9) between the surface of coating and water droplet formed. The corrosion resistance property is unswervingly linked to higher CA values. Among the different weight ratios of EBCE coatings, EBCE (1:1) showed higher CA value (77.47°). The incorporation of 0.2 wt% and 0.3 wt% FGO enhanced the CA values (90.59° and 95.19°), whereas, the CA values of EBCE/FGO (0.1 wt%) and EBCE/FMWCNT (0.1 wt%) were dropped to 73.33° and 67.79°, respectively. Noteworthily, EBCE/FMWCNT (0.3 wt %) possessed highest CA values (113.10°), suggesting its elevated hydrophobicity compared to all other samples. This is attributed to the uniform distribution of FMWCNT, aids to achieve low surface energy, equal stress distribution throughout the coating. Further the presence of hydrophobic functional groups such as aromatic group in eugenol benzoxazine, tertiary butyl group in modified nanofillers, and polyphenolic group in curcumin promoting its hydrophobicity even after saline immersion duration (supplementary information Fig. S5). On the other, uneven dispersion of fillers can agglomerate and form uneven regions assisting in absorption of water reducing contact angle. Further, the natural hydrophobic nature of the curcumin in its epoxidized form plummeting the absorption of water and assisting in filling the plausible

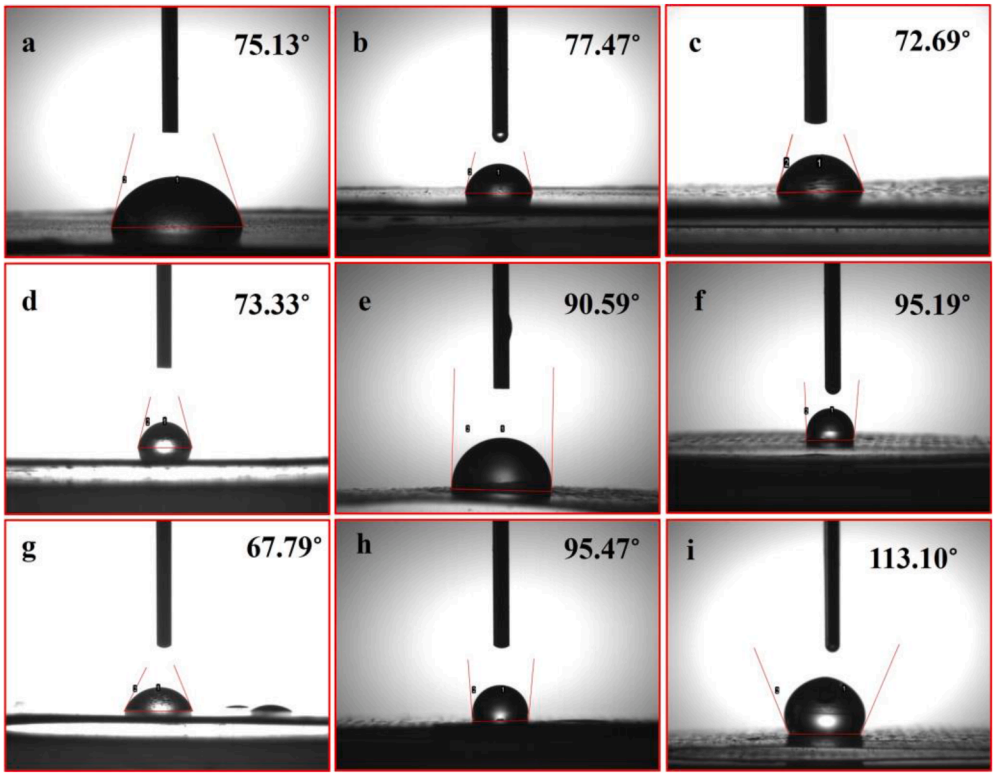

Fig. 9. Contact angle results of (a) EBCE (2:1), (b) EBCE (1:1), (c) EBCE (1:2) coatings, (d) 0.1 wt%, (e) 0.2 wt%, (f) 0.3 wt% FGO incorporated EBCE coating, (g) 0.1 wt%, (h) 0.2 wt%, (i) 0.3 wt% FMWCNT incorporated EBCE coated MS surface.

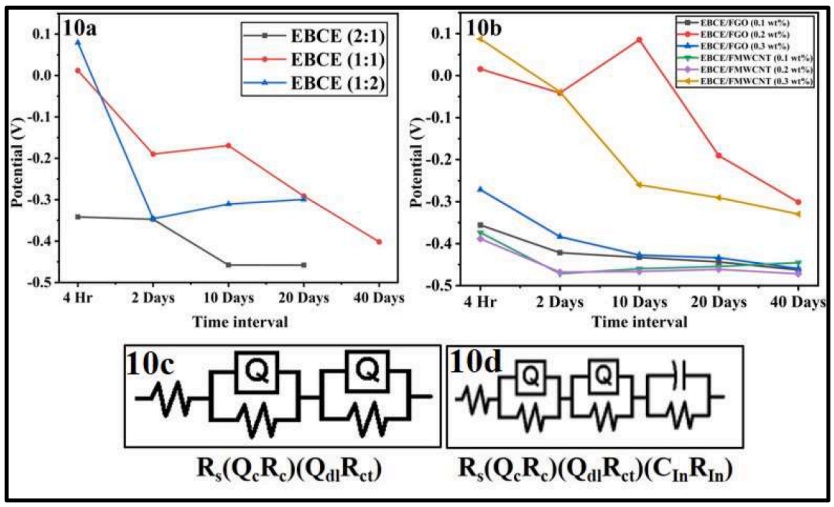

Fig. 10. OCP variations of different ratios of EBCE and various wt% of FGO and FMWCNT incorporated EBCE (1:1) coatings. Fitted electrochemically equivalent circuits (c) $R_s(Q_cR_c)(Q_{dl}R_{ct})$, and (d) $R_s(Q_cR_c)(Q_{dl}R_{ct})(C_{In}R_{In})$.

voids in the coating and enhances water repellence nature. The hydrophobicity of the coatings follows the order, EBCE/FMWCNT (0.3 wt%) > EBCE/FMWCNT (0.2 wt%) > EBCE/FGO (0.3 wt%) > EBCE/FMWCNT (0.2 wt%) > EBCE (1:1) > EBCE/FGO (0.1 wt%) > EBCE (1:2) > EBCE (2:1).

3.9. Corrosion studies

3.9.1. Electrochemical impedance spectroscopy

The electrochemical impedance spectroscopy (EIS) technique was employed to estimate the anti-corrosion evaluation of EBCE with different weight ratios of EB and CE resin, and with different wt% of FGO and FMWCNT incorporated EBCE coatings at 4 hrs, 3 days, 10 days, 20 days and 40 days. Prior to this, open circuit potential (OCP) was conducted to evaluate the corrosion susceptibility and steadiness attained between the working electrode and the saline environment for all the samples. The OCP value of EBCE (1:1) was gradually declining in the range of 0.012 V to -0.291 V from initial to 40th day of immersion, whereas, the OCP values of EBCE (2:1) and EBCE (1:2) are found at high negative potentials on increasing the immersion duration, witnessing a radical fall over time (Fig. 10a). The 0.2 wt% of FGO and 0.3 wt% of FMWCNT inducted EBCE coatings showed high positive OCP values (0.015 V, -0.041 V and 0.087 V, -0.038 V) in the initial period of immersion (Fig 10b), pointing at high corrosion resistance. The OCP of

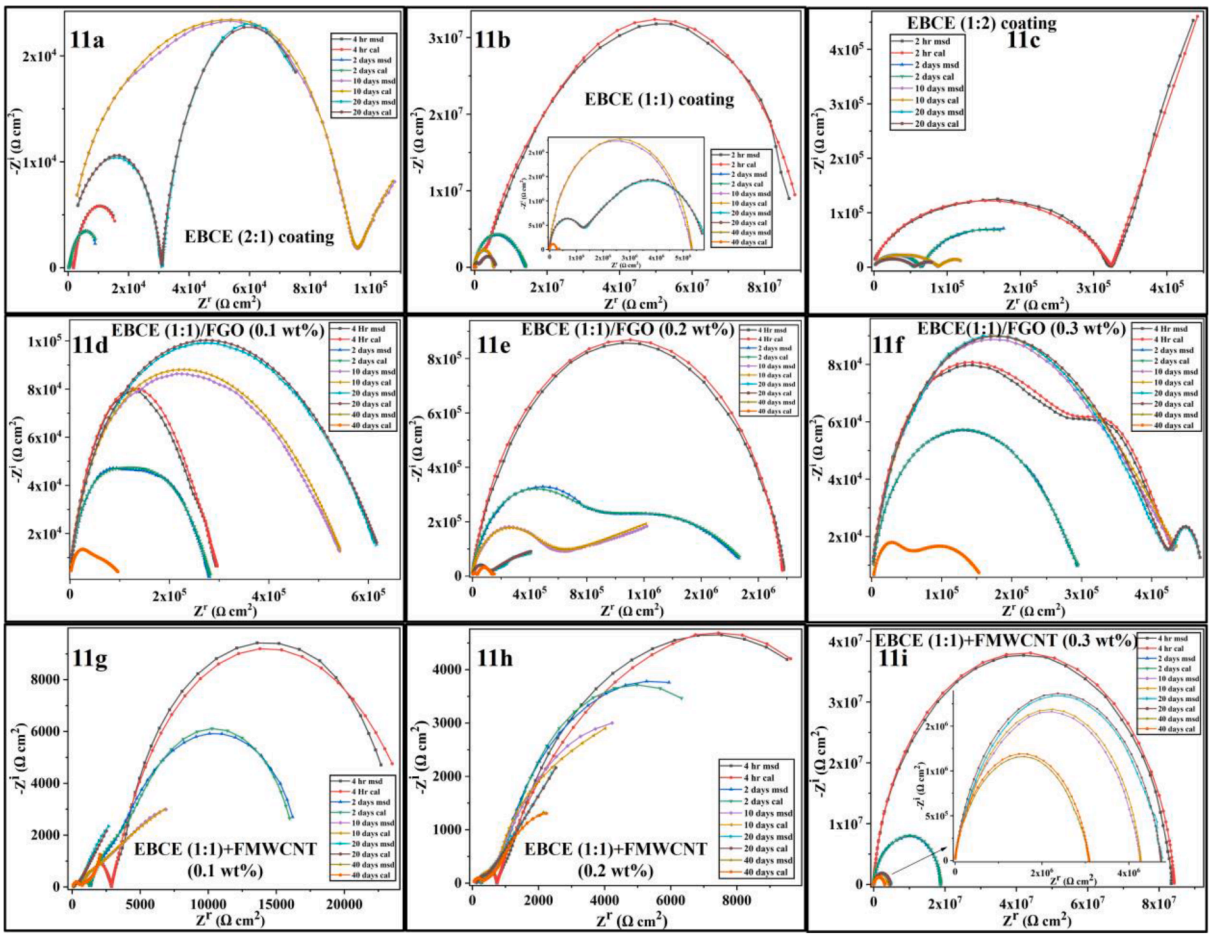

Fig. 11. Nyquist plots of (a) EBCE (2:1), (b) EBCE (1:1), (c) EBCE (1:2) coatings. EBCE (1:1) coating with different wt% of FGO (d) 0.1 wt%, (e) 0.2 wt%, (f) 0.3wt % and different wt % of FMWCNT (g) 0.1 wt% (h) 0.2 wt% (i) 0.3 wt%.

other samples are found in the range of -0.150 V to -0.400 V, and dropped over time indicating their susceptibility to corrosion. The EIS was conducted in the frequency range of 0.01 Hz - 0.1 MHz with a three-electrode system (Ag/AgCl reference electrode, Pt - wire counter electrode, coated MS specimen as working electrode). The coated samples were immersed in the saline medium with the unit area exposure and the remaining regions were closed entirely with an insulation tape.

The anti-corrosion phenomenon of the coatings was assessed with Nyquist-Bode plots. The nyquist plot is a graphical representation of real impedance (Z^r) on X-axis and imaginary impedance (- Z^i) on Y-axis. They are interpreted by the nature of altitude, breadth of the semi-circle, semi-circular arc, diffusion tail, and single/double time constant development, while, the bode plots are the impedance modulus at lower frequency ($|Z|_{0.01Hz}$). The nyquist plots of EBCE (2:1) and EBCE (1:2) coatings showed a characteristic diffusion tail at the initial saline soaking period with decreasing peak height (Fig. 11a and 11c). As perceived, the 1:1 EBCE displayed highest impedance and semi-circular arc on initial days, followed by single time constant, and complete semi-circle compared to other weight ratios of EBCE coatings, indicating its notable corrosion resistance at 10^{th} and 20^{th} day of immersion (Fig. 11b). The bode plots showed 7 to 6.5 counts for EBCE (1:1) coating depicting its high resistance to electrolyte permeation with higher capacitive loop and phase angle ($\theta_{0.1MHz}$) above -80°. The EBCE with 1:2 and 2:1 ratios offered lesser resistance as seen with lower $|Z|_{0.01Hz}$ values (4.5 to 5.5) and lower capacitive range with $\Theta_{0.1MHz}$ around -60°. Additionally, the second time constant at around -45° was witnessed as seen in Fig. 12(a-c). This could be ascribed to the insufficient molecular interaction between the EB and CE, and also uneven distribution of composite materials with deficient crosslinking throughout the coatings. This leads to deficient crosslinking and increase the pores in the coating and paving easier path for the electrolytic movement to initiate corrosion. From the above results, the EB and CE at 1:1 weight ratio has been opted as an ideal composition for evaluating the effects of different weight percentages of FGO and FMWCNT in the EBCE coating matrix.

The 0.1 wt% and 0.3 wt% of FGO inducted EBCE (1:1) coatings showed a complete and broader semi-circle with single time constant. On 20^{th} and 40^{th} days of soaking, the crescent heights decreased with depressed semicircle (Fig. 11 d and f), depicting the constant attacks of corrosive agents causing fatigue in coatings, and thus failed to provide durable anti-corrosion performance. The EBCE/FGO (0.2 wt%) coating developed a strong diffusion tail with an angle of 45° from 10^{th} day of saline immersion and further showed 2-time constants on 40^{th} day of immersion with least resistance as seen in the Fig. 11e. In addition, the bode-phase plots exhibited lesser capacitive range, with more than one one-time constant, due to the lesser compatibility of the FGO in the coating matrix leading to agglomeration of GO sheets, pointing at the deterioration of coating due to the formation of passive oxide layer [74]. The nyquist plots of 0.1 wt% and 0.2 wt% FMWCNT incorporated EBCE (1:1) coatings during initial immersion period (4 hrs and 2 days), displayed the diffusion tails in lower frequency range as shown in Fig. 11g and h, attributing to least corrosion resistance due to the delamination and permeation of Na^+, Cl^- ions through the coatings. However, the EBCE/FMWCNT (0.3 wt%) coating showed a larger complete semi-circle with higher impedance. The phase angles were consistent throughout the soaking period with larger capacitive range, indicating the capacitance behaviour of the coating (Fig. 11i). Bode plots exhibited fine

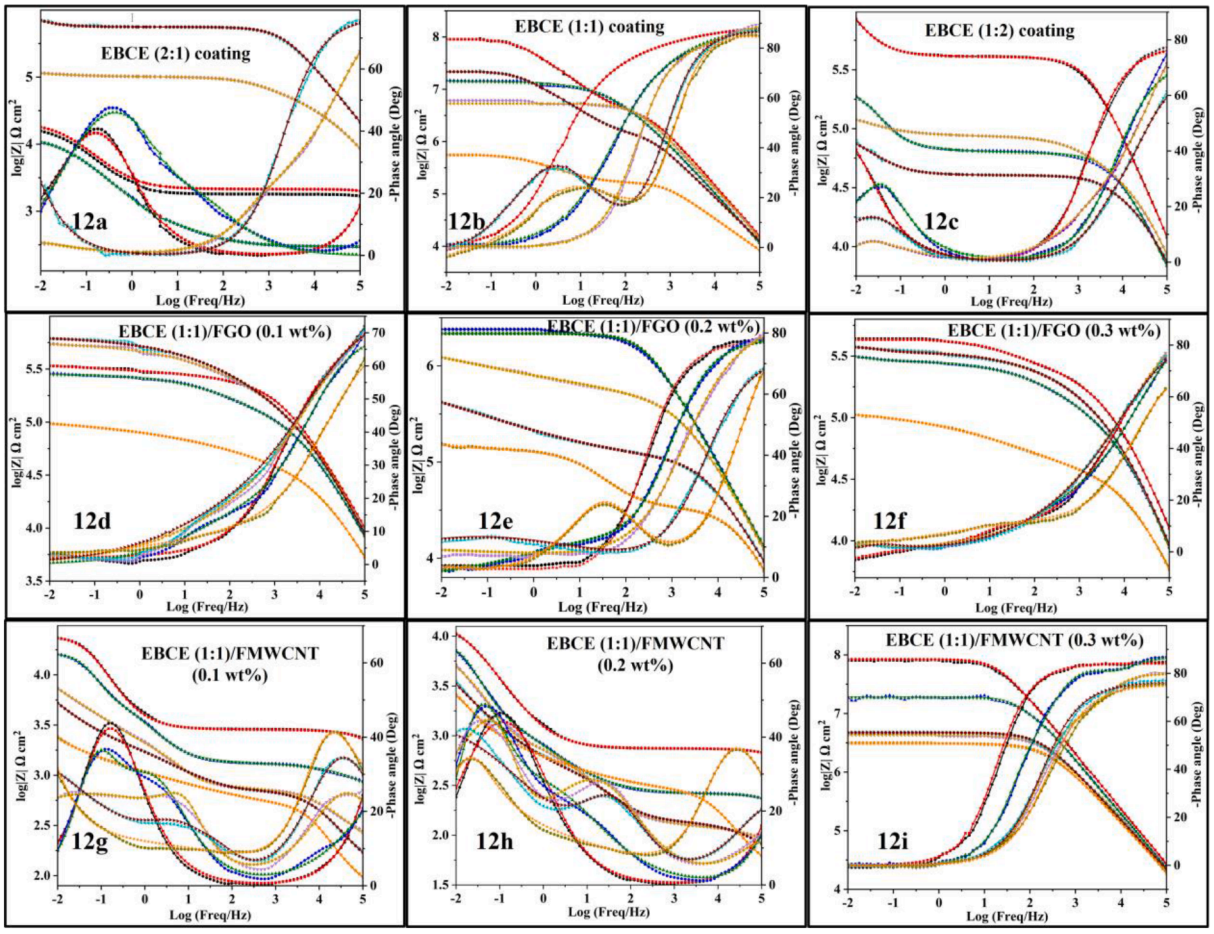

Fig. 12. Bode-Phase plots of (a) EBCE (2:1), (b) EBCE(1:1), (c) EBCE (1:2) coatings, EBCE (1:1) coating with different wt% of FGO (d) 0.1 wt%, (e) 0.2 wt%, (f) 0.3 wt % and different wt % of FMWCNT (g) 0.1 wt% (h) 0.2 wt% (i) 0.3 wt%.

coating resistance even on moving to higher frequency (up to 2 counts) (Fig. 12i). Thus, 0.3 wt% of FMWCNT inducted EBCE coating resisting the corrosive ions to pass through compared to all other coatings.

The detailed quantification of anti-corrosion properties of the coatings was estimated using electrochemical parameters by fitting suitable equivalent circuits. During initial days, $R_s(Q_cR_c)(Q_{dl}R_{ct})$, and on later days, $R_s(Q_cR_c)(Q_{dl}R_{ct})(C_{In}R_{In})$ circuits (Fig. 10 c,d) are fitted to measure the impedance data, and the rendered results are presented in Tables 1 and 2. The χ^2 values resulting from fitting all the measured data of the coatings were found to be below 0.001, indicating admirable agreement with measured (msd) and calculated (cal) data [75]. Here R_c and R_{ct} are the coating resistance and charge transfer resistance, respectively, these parameters are directly related to the anti-corrosive behaviour of the coatings. Q_c and Q_{dl} are the capacitance of coating and double layer capacitance introduced as a constant phase elements due to non-ideal behaviour of the coating, which are calculated using Eq 3, where Y_o is the admittance to solution and 'n' is the exponent ranging between $0 \leq 1$. The capacitance of the coating conveys the coating ability to retain the water molecule to reach the MS surface.

$$Q_{c/dl} = \frac{\left(Y_0 \times R_{c/ct}\right)^{1/n}}{R_{c/ct}} \tag{3}$$

During initial soaking period (4 Hr), the 2:1, 1:1, and 1:2 ratios of EBCE coatings showed the R_c values of 1.91×10^4 Ω cm^2, 9.24×10^7 Ω cm^2, and 1.92×10^4 Ω cm^2, respectively. The highest R_{ct} value (4.28×10^7 Ω cm^2) was seen for 1:1 coating, showcasing the formation of impermeable layer, while the other coatings showed lesser resistance to corrosive agents. As the soaking period increased, the R_c and R_{ct} values of 2:1 and 1:2 ratios were decreased to 4.59×10^4 Ω cm^2, 8242 Ω cm^2 and 6999 Ω cm^2, 9241 Ω cm^2, respectively. The fluctuation in R_{ct} value of EBCE (2:1) during 10th and 20th days of soaking is due to the passive protection provided by the oxide layer [76]. The R_c and R_{ct} values of 1:1 ratios were found to be around 10^6 Ω cm^2 - 10^5 Ω cm^2 of up to 20th day of immersion indicating its coating intactness despite longer saline exposure. This exceptional resistance of coating against the corrosive medium validating the fine crosslinking leading to the dense arrangement of the matrix which ceases the electrolyte permeability and allocates for high capacitance behaviour of the EBCE (1:1) coating with lower and more negative Q_c and Q_{dl} values [77,78]. The different wt% of FGO incorporated EBCE coatings exhibited the R_c values of around 10^6 Ω cm^2 - 10^4 Ω cm^2 and their coating capacitance (Q_c) increased over time. The Q_c is inversely related to water intake of the coating. The higher and negative Q_c values directly attribute to coatings ability to resist the water movement through the coatings. The Q_c and Q_{dl} values of EBCE at 2:1 and 1:2 ratios displayed increasing trend from initial days to final immersion duration (2.99×10^{-10} F/cm^2, 5.93×10^{-11} F/cm^2, to 2.65×10^{-6} F/cm^2, 8.59×10^{-7} F/cm^2). This abrupt decline in Q_c and Q_{dl} values over time could be due to the water intake through the coatings [79]. The fluctuations in the Q_{dl} values of EBCE coatings and FGO incorporated EBCE coating indicate the higher interfacial activity between the metal and the coating junction, resulting in loss of corrosion protection property of the coatings. The 0.1, 0.2 and 0.3 wt% s of FMWCNT incorporated EBCE coatings exhibited the R_c values of 2.38×10^4 Ω cm^2, 1.61×10^4 Ω cm^2, 9.25×10^7 Ω cm^2, respectively, conveying greater corrosion resistance at 0.3 wt% in the initial immersion period. It is supported by its highest R_{ct} value (2.76×10^8 Ω cm^2) compared to other

Table 1
Electrochemical parameters of different ratios of EBCE coatings.

Sample	Immersion time	Q_c (F/cm^2)	R_c (Ω cm^2)	Q_{dl} (F/cm^2)	R_{ct} (Ω cm^2)	χ^2 values
	4 hrs	2.99×10^{-10}	1.91×10^{4}	0.00010	1909	5.73×10^{-4}
EBCE (2:1)	2 days	0.0002	1.16×10^{4}	4.66×10^{-5}	688	1.48×10^{-4}
	10 days	2.8×10^{-7}	1.61×10^{5}	0.00036	2.31×10^{5}	2.04×10^{-4}
	20 days	7.78×10^{-6}	1.34×10^{4}	6.15×10^{-5}	5.51×10^{5}	3.35×10^{-4}
	40 days	2.65×10^{-6}	4.59×10^{4}	3.64×10^{-5}	6999	1.72×10^{-4}
	4 hr	1.33×10^{-10}	9.24×10^{7}	7.98×10^{-10}	4.28×10^{7}	4.70×10^{-4}
EBCE (1:1)	2 days	1.73×10^{-10}	9.53×10^{6}	1.61×10^{-10}	5.02×10^{6}	7.26×10^{-4}
	10 days	1.61×10^{-10}	4.97×10^{6}	1.21×10^{-7}	5.72×10^{6}	9.33×10^{-5}
	20 days	1.22×10^{-9}	1.31×10^{6}	6.70×10^{-9}	1.96×10^{6}	3.01×10^{-4}
	40 days	1.05×10^{-9}	5.96×10^{5}	4.92×10^{-7}	3.58×10^{5}	5.16×10^{-4}
	4 hr	5.93×10^{-11}	1.92×10^{5}	3.11×10^{-5}	3.25×10^{5}	2.04×10^{-4}
EBCE (1:2)	2 days	4.28×10^{-10}	9362	3.06×10^{-7}	1.60×10^{4}	1.14×10^{-4}
	10 days	4.75×10^{-8}	9018	1.90×10^{-6}	777.5	9.07×10^{-4}
	20 days	8.59×10^{-7}	8242	0.0002	9241	8.44×10^{-4}

Table 2
Electrochemical parameters of FGO and FMWCNT inducted EBCE coatings.

Sample	Immersion time	Qc (F/cm^2)	R_c (Ω cm^2)	Qdl (F/cm^2)	R_{ct} (Ω cm^2)	χ^2 values
	4 hrs	2.33×10^{-10}	4.90×10^{5}	8.47×10^{-11}	1.83×10^{4}	9.32×10^{-4}
EBCE (1:1)/ FGO (0.1 wt %)	2 days	4.83×10^{-10}	2.85×10^{5}	1.39×10^{-9}	1.25×10^{5}	4.82×10^{-4}
	10 days	2.59×10^{-10}	5.67×10^{5}	2.61×10^{-8}	6.78×10^{4}	6.86×10^{-4}
	20 days	2.87×10^{-10}	6.45×10^{5}	1.61×10^{-6}	7.86×10^{3}	1.38×10^{-4}
	40 days	3.94×10^{-9}	7.77×10^{4}	2.56×10^{-6}	1.10×10^{4}	1.64×10^{-4}
	4 hrs	2.76×10^{-10}	2.17×10^{6}	8.98×10^{-13}	1.17×10^{5}	5.34×10^{-4}
EBCE (1:1)/ FGO (0.2 wt %)	2 days	1.61×10^{-9}	1.68×10^{5}	2.99×10^{-6}	3.35×10^{6}	6.81×10^{-4}
	10 days	1.57×10^{-9}	5.29×10^{5}	4.39×10^{-6}	2.81×10^{5}	1.67×10^{-4}
	20 days	5.05×10^{-8}	1.04×10^{4}	0.0234	1.06×10^{5}	1.18×10^{-4}
	40 days	8.33×10^{-5}	1.63×10^{4}	3.44×10^{-8}	5.79×10^{4}	1.51×10^{-4}
	4 hrs	1.22×10^{-10}	4.54×10^{5}	2.39×10^{-10}	0.00999	4.48×10^{-4}
EBCE (1:1)/ FGO (0.3 wt %)	2 days	1.30×10^{-10}	3.32×10^{5}	2.45×10^{-10}	1.66×10^{4}	5.58×10^{-4}
	10 days	0.0215	3.17×10^{5}	5.77×10^{-10}	5.46×10^{4}	2.28×10^{-4}
	20 days	1.18×10^{-8}	1.16×10^{5}	2.30×10^{-9}	9.59×10^{5}	2.39×10^{-4}
	40 days	3.70×10^{-7}	1.71×10^{5}	1.75×10^{-9}	3.65×10^{4}	1.12×10^{-4}
	4 hrs	4.93×10^{-7}	2.38×10^{4}	2.46×10^{-10}	2905	6.22×10^{-4}
EBCE (1:1)/ FMWCNT (0.1wt%)	2 days	6.06×10^{-5}	3929	6.44×10^{-10}	1346	6.67×10^{-4}
	10 days	2.95×10^{-7}	2450	0.0014	1.33×10^{4}	3.78×10^{-4}
	20 days	3.56×10^{-7}	1470	0.0012	1599	1.99×10^{-4}
	40 days	6.88×10^{-7}	346	0.0016	1.36×10^{4}	4.06×10^{-4}
	4 hrs	1.27×10^{-10}	1.61×10^{4}	1.62×10^{-10}	9750	6.33×10^{-4}
EBCE (1:1)/ FMWCNT (0.2 wt %)	2 days	8.11×10^{-9}	1.07×10^{4}	2.24×10^{-7}	0.0080	8.93×10^{-4}
	10 days	8.37×10^{-9}	4730	1.39×10^{-7}	0.0011	1.10×10^{-4}
	20 days	1.91×10^{-8}	111.2	2.72×10^{-5}	307.2	9.40×10^{-4}
	40 days	8.20×10^{-7}	43.8	9.36×10^{-8}	208.8	2.25×10^{-4}
	4 hr	9.54×10^{-11}	9.25×10^{7}	3.01×10^{-10}	2.76×10^{8}	9.04×10^{-4}
EBCE (1:1)/ FMWCNT (0.3 wt %)	2 days	2.11×10^{-10}	3.64×10^{6}	3.09×10^{-10}	1.52×10^{7}	2.23×10^{-4}
	10 days	3.88×10^{-10}	1.37×10^{6}	3.14×10^{-10}	4.14×10^{6}	2.53×10^{-4}
	20 days	1.91×10^{-10}	4.74×10^{6}	2.78×10^{-12}	1.02×10^{6}	3.22×10^{-4}
	40 days	2.13×10^{-10}	3.09×10^{6}	3.17×10^{-12}	6.00×10^{6}	3.69×10^{-4}

FMWCNT inducted EBCE coatings (2905 Ω cm^2 and 9705 Ω cm^2). On prolonged immersion, the EBCE/FMWCNT (0.3 wt%) displayed a consistent R_c and R_{ct} values at around 10^6 Ω cm^2 along with Q_c of 2.13×10^{-10} Ω cm^2 even at 40th day of immersion contributing to highest contact angle. All the variations of R_c and R_{ct} trends of the coatings throughout the immersion is presented in supplementary information Fig. S6. Fascinatingly, its Q_{dl} values showed high negative values of around 10^{-10} to 10^{-12} F/cm^2 validating strong barrier performance, decreased wettability, intact coating integrity, and least interfacial activity [80,81]. Also, the bode plots of EBCE (1:1)/FMWCNT (0.3 wt%) displayed clear and complete capacitive arc formation even on moving to higher frequency, which is supporting the durability of the coatings [82,83]. The dependable anti-corrosion performance of EBCE (1:1)/FMWCNT (0.3 wt%) coating was found to be superior to some of the conventional as well as bio-based anti-corrosion coatings, and their comparative chart is presented in the Table 3. The incorporation of optimum quantity of FMWCNT results in its fine dispersion, along with the synergistic effect of CE and tertiary butyl methyl groups of FMWCNT, boosted the barrier performance in the coating matrix. Further, the hydrophobicity of the coating is enhanced which is reflected by its high CA value. The high-water repellent property of EBCE/FMWCNT (0.3 wt%) supplementing the increased crosslinking and also the formation of denser network in the coating matrix.

3.10. Salt spray analysis

The neutral salt spray analysis (SSA) was conducted for 288 hrs using 5 wt% saline solution at pH 7, and maintaining the temperature of salt spray chamber at 28 °C. The images are procured for every 48 hrs interval. The accelerated corrosion evaluation was carried out by ASTM B117-19 standard method. The edges of the prepared EBCE (2:1), EBCE (1:1), EBCE+FGO (0.1 wt%), EBCE+FGO (0.3 wt %), EBCE+FMWCNT (0.1 wt %), and EBCE+FMWCNT (0.3 wt%) coatings are sealed using insulation tape and the coatings are artificially scratched before subjected to SSA as shown in Fig. 13. Initially, SSA witnessed no changes in its physical nature of the coatings. After 144 hrs, the EBCE (2:1), FGO incorporated EBCE, and EBCE+FMWCNT (0.1 wt %) coatings were infested with corrosion blisters, and chipping off of the coatings was seen, indicating poor adhesion and the corrosive agents were easily channelled through the coatings. On the other, the EBCE (1:1) and 0.3 wt% of FMWCNT inducted EBCE (1:1) coatings restricted corrosion to the artificially scratched site and showed no signs of spread through the coatings even after 288 hrs. The ideal weight ratio of the core matrix composition, the optimum amount of nanofiller compatibility in forming uniform dense network, and strong intermolecular bonding, contributes for increased anti-corrosion performance of EBCE+FMWCNT

Table 3
Comparison of the corrosion protection results with other reported coating systems.

Sl. no	Coating system	R_{ct} in (Ω cm^2)	Contact angle	Reference
1	Phthalimide/polybenzoxazine (PBz)	1.29×10^6	105° to 98°	[84]
2	0.25 wt% f-MWCNT/Pin-epoxy	3.76×10^5	91°	[85]
3	0.5 wt% FGO/epoxy	1.11×10^5	-	[86]
4	Waterborne polyurethanes	1.37×10^6	70.5°	[87]
5	MTMS-APTMS/epoxy	4.53×10^5	75°	[88]
6	EPPyNG2	5.61×10^6	-	[89]
7	TEOS-PBz-210	3.77×10^5	105°	[90]
8	PBz/SiO_2	5.12×10^6	89°	[91]
9	Silane modified Bz/TEOS	10^5	103°	[92]
10	Beeswax/GO (0.3 wt%)	8.77×10^4	107°	[93]
11	Polycaprolactone/FGO	8.94×10^5	106°	[94]
12	Curcumin octadecyl amine based Bz	2.34×10^4	-	[95]
13	Capsaicin based PBz	10^5	-	[96]
14	EBCE (1:1)/FWCNT (0.3 wt%)	6.00×10^6	113.10°	Current work

(0.3 wt%) coating.

Further, the optical images showed in Fig. 14 validate the thorough spread of corrosion underneath the coating surface for EBCE (1:2), and FGO and 0.1 wt% FMWCNT incorporated EBCE coatings. The yellow-coloured markings on the coatings showed the rust deposition and the bubbles around the coating are due to the saline infusion and lesser adhesive strength. In the meantime, EBCE/FMWCNT (0.3 wt%) coating showed lesser spread of the corrosion compared to all other samples indicating its strong binding to the MS substrate.

3.11. Crosshatch adhesion test

The long-term corrosion barrier performance can be corroborated to cross hatch adhesion test and adhesion rating, in combination with other properties such as coating integrity and coating resistance. The barrier property of the coatings shows rapid decrease in the impedance over time due to poor adhesion. Higher adhesion rating attributes to strong interfacial bonding between the MS substrate and coating. The strong adhesion of the coating assists to preserve coating continuity, preventing delamination, bubbling, and cracking of the coating which in turn evading the moisture and corrosive agents' movement. While the poor adhesion enables rust formation beneath the coating, causing bubbling and lift off (depicted in Fig. 13 and 14 of salt spray analysis and optical images). Therefore, strong adhesion augments durability, paired with excellent barrier property and the chemical properties of the coating materials [97–99]. The crosshatch adhesion test was conducted by following ASTM D 3359 method to identify the intactness and adhesion affinity of the coatings to MS substrate. An ideal barrier performance requires stronger adhesion between the steel and the coating material [100]. The shedding and detachment imparity of the coatings were related with the reference chart as reported by Harsha *et al.* [101]. The EBCE (1:2), 0.1 wt%, and 0.3 wt% FGO incorporated EBCE coatings displayed poor adhesion property, and are peeled off rapidly when scratched. The bits of coating pieces are found latched on the squared regions of the tape randomly, and are falling in the adhesion rating of 0B (Fig. 15 a,b,e). Thus, the least adhesive nature of the FGO incorporated EBCE coatings fail to provide reliable barrier performance. The EBCE (1:1) showed resistance to peeling and the coating was found to be intact. The tape peeling results showed few portions of the coating removal on the edges and intersectional areas, observing 5% - 15% area removal with 4B rating (Fig. 15c). The EBCE/FMWCNT (0.3 wt%) displayed stupendous adhesion with <6 % area loss. The edges are virtually smooth and the least pieces of coating were seen on the tape markings,

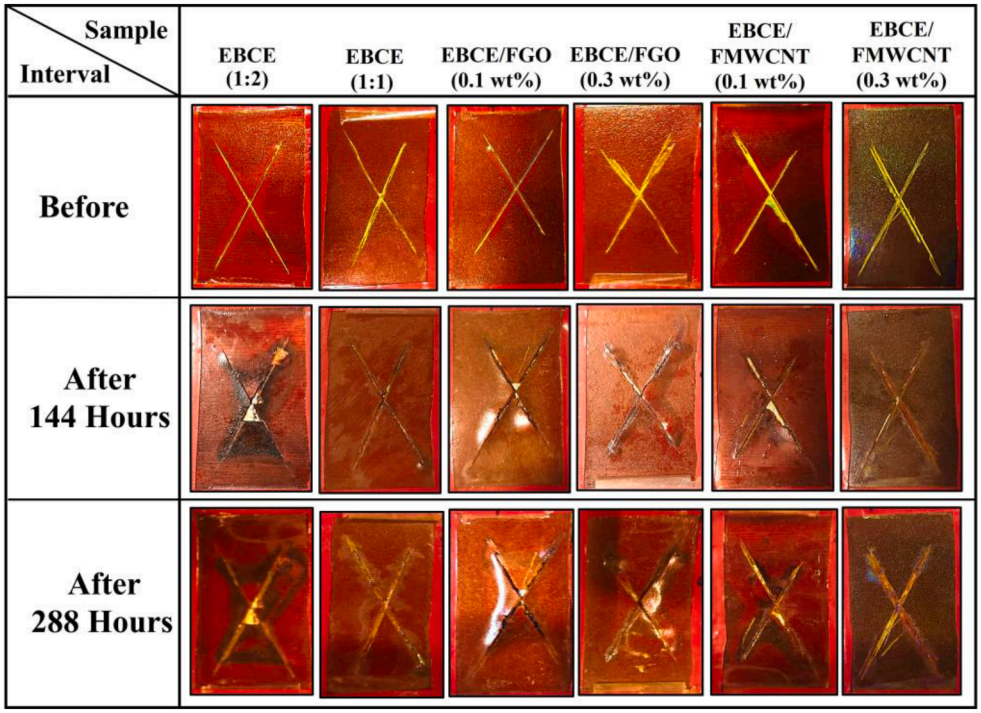

Fig. 13. Salt spray analysis of scratched MS coated samples of EBCE (1:2), EBCE (1:1), 0.1 wt%, 0.3 wt% FGO inducted EBCE coating, and 0.1 wt%, 0.3 wt% FMWCNT inducted EBCE coatings.

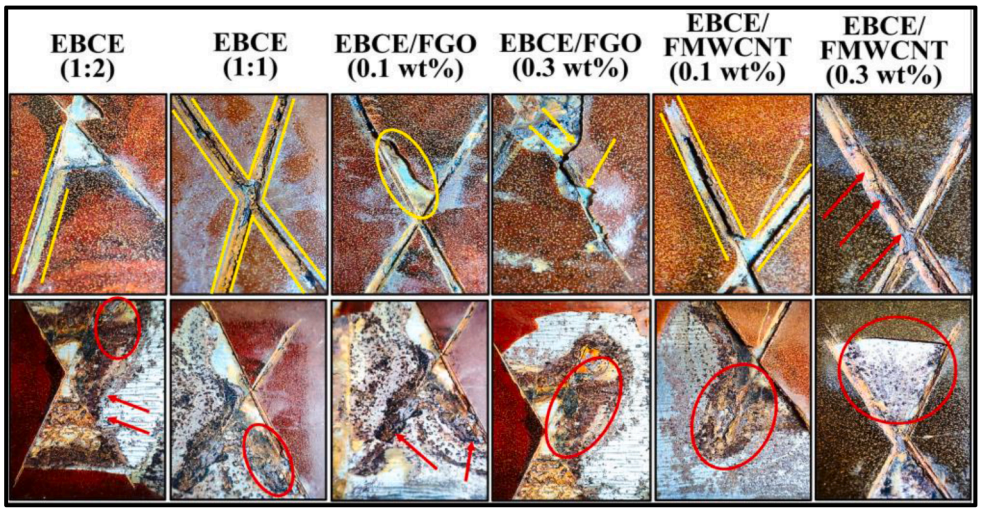

Fig. 14. Optical images of scratched MS coated samples of EBCE (1:2), EBCE (1:1), 0.1 wt%, 0.3 wt% FGO inducted EBCE coatings, and 0.1 wt%, 0.3 wt% FMWCNT inducted EBCE coatings after salt spray analysis.

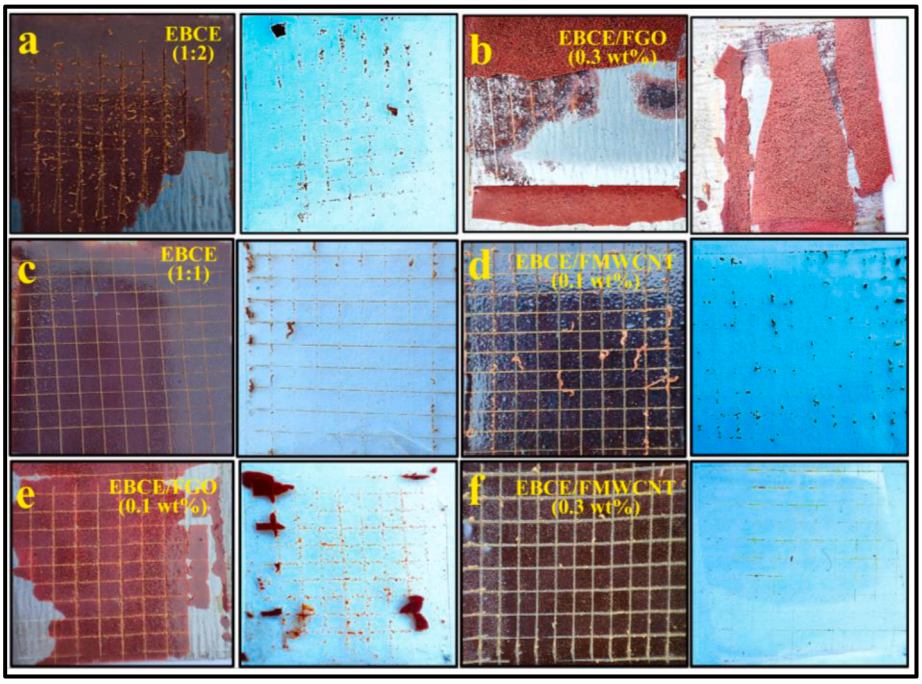

Fig. 15. Crosshatch images of (a) EBCE (1:2), (c) EBCE (1:1), (e) 0.1 wt%, (b) 0.3 wt% FGO inducted EBCE coatings, and (d) 0.1 wt%, (f) 0.3 wt% FMWCNT inducted EBCE coatings.

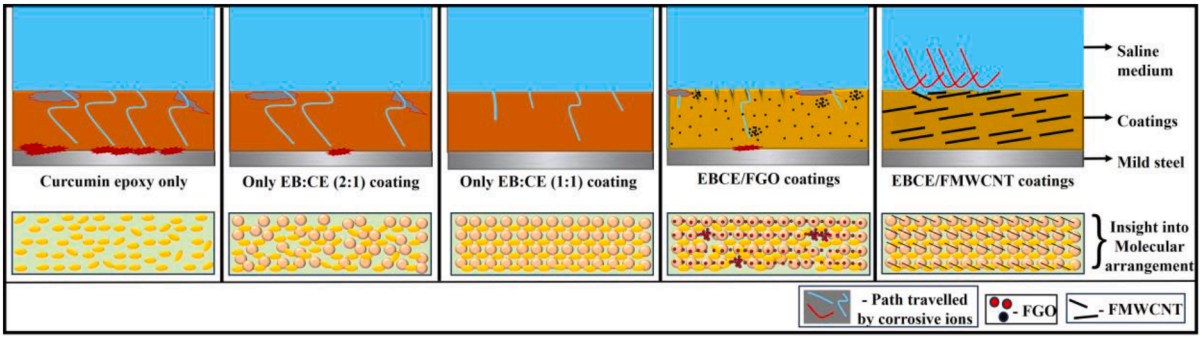

Fig. 16. Pictorial representation depicting the role of curcumin epoxy, EBCE, and different nanofillers on corrosion protection mechanism.

validating its virtuous crosslinking network and filler compatibility with the adhesion rating of 5B to 4B.

3.12. Corrosion resistance mechanism of coatings

In general, the nitrogen atom linkages and the presence of aromatic group in the benzoxazine assists in achieving high temperature resistance and also low shrinkage on curing [102–104]. The functionalized carbon based nanofillers act as ideal filler materials in the coating matrix due to their high aspect ratio, surface area, and amplified dispersibility. However, excess/deficient amount of nanofiller induction causes agglomeration and inability to interact with core matrix, and initiating the development of cracks in the coatings [105]. Based on the EIS studies, it was ascertained that the EBCE coating with the incorporation of chemically modified MWCNT showed high corrosion resistance compared to clean EBCE and FGO inducted EBCE coatings (Fig. 16). The modified MWCNT generally possess high aspect ratio and acting as efficient filler material due to its long tubular 1D geometry, enabling its torturous paths, uniform distribution of stress in the coating matrix, and hence hindering the diffusion of corrosive agents. The 2D planar morphology of GO could agglomerate even after modification due to the strong van der Waals forces, and forming cracks and defects, thereby reducing barrier properties of the coatings. Better conductivity of MWCNT facilitates uniform distribution of particles in the coating matrix and assisting to form strong covalent and hydrogen bonding interaction with EBCE. The amine functionalized MWCNT improves interfacial adhesion, and reduces nanofiller separation from the core matrix, resulting in consistent and tough coating as witnessed in the adhesion results. Whereas in FGO, the presence of oxygen containing functionalities promotes water intake and reducing its protection ability [106–108]. The higher nitrogen content in the FMWCNT compared to FGO further contributed in increasing the filler and matrix compatibility and achieving its uniform dispersion of nanofiller in the coating matrix. Further, the decreased pinholes and defects resulted in increased R_{ct}, CA and adhesion ratings of the EBCE/FMWCNT (0.3 wt%) coating. Hence, the 0.3 wt% of FMWCNT in the EBCE coating denied the entry of corrosive ions due to its compatibility with CE resin, and also the presence of tertiary butyl methyl group in the nano filler tandemly work to repel the water molecules in the core matrix, and impede the spreading of corrosion phenomenon as seen in SSA. Further, the FMWCNT occupies and sealed the unreachable gaps in the coating resulted in increased CA values. The sub-optimal concentrations of EBCE and FMWCNT resulted in agglomeration, weaker inter molecular bonding, and poor adhesion. Further, due to their hydrophilic nature, the cracks are developed and widened, making easier paths for corrosive ions movements [109].

4. Conclusion

A non-toxic and sustainable EBCE anti-corrosion coating material is developed with different weight ratios of EB and CE. The EB is synthesized by one pot Mannich type condensation reaction and CE resin is prepared by the epoxidation of curcumin. GO and MWCNT are chemically modified with 5-amino-2, 4-di-tert-butylphenol and confirmed by XRD, FT-IR, Raman spectroscopy, FE-SEM, EDX, TGA, TEM, SAED and XPS techniques. The corrosion barrier performances of various weight ratios of EBCE coatings, and different wt% of FGO and FMWCNT inducted EBCE coatings are evaluated using EIS and SSA. The surface morphology, adhesion, and hydrophobic character of the coated MS samples are estimated by AFM, crosshatch adhesion test and CA measurements. Corrosion analysis and hydrophobic character revealed that, the 0.3 wt% FMWCNT dispersed EBCE (1:1) coating showed best anti-corrosion performance compared to all other coatings with the R_c value of 3.09×10^6 Ω cm^2 and CA value of 113.50° at 40^{th} day of immersion in 3.5 wt% NaCl solution. The ideal weight ratio of the core matrix composition and the optimum amount of nanofiller compatibility contributes for uniform dense network, strong intermolecular bonding, and increased crosslinking in the EBCE/FMWCNT (0.3 wt%) coating. The present study provides an insight into an innovative application of a new class of eco-friendly and sustainable material in the corrosion protection of marine equipment's and industrial piping systems. Further, the EBCE can be a futuristic hybrid smart coating material in the area of corrosion prevention of metals.

CRediT authorship contribution statement

Malavalli Chidanandakumar Hithesh: Writing – review & editing, Writing – original draft, Visualization, Validation, Software, Project administration, Methodology, Investigation, Funding acquisition, Formal analysis, Data curation, Conceptualization. **Yadavanahalli Mahalingaiah Harsha:** Formal analysis. **Kikkeri Narasimha Shetty Mohana:** Writing – review & editing, Validation, Supervision, Investigation, Formal analysis. **Muralidharan Sreelakshmi:** Formal analysis. **Mysore Chandru Sunil Kumar:** Formal analysis.

Declaration of competing interest

The authors declare that they have no known competing financial interests or personal relationships that could have appeared to influence the work reported in this paper.

Supplementary materials

Supplementary material associated with this article can be found, in the online version, at doi:10.1016/j.surfin.2025.107150.

Data availability

Data will be made available on request.

References

[1] D. Thomas, R. R, E. Philip, R. Sindhu, S.B. Ulaeto, A. Pugazhendhi, M.K. Awasthi, Developments in smart organic coatings for anticorrosion applications: a review, Biomass Convers Biorefin 12 (2022) 4683–4699, https://doi.org/10.1007/s13399-022-02363-x.
[2] M. Faccini, L. Bautista, L. Soldi, A.M. Escobar, M. Altavilla, M. Calvet, A. Domènech, E. Domínguez, Environmentally Friendly Anticorrosive Polymeric Coatings, Applied Sciences 11 (2021) 3446, https://doi.org/10.3390/app11083446.
[3] S.K. Dhawan, H. Bhandari, G. Ruhi, B.M.S. Bisht, P. Sambyal, Corrosion Preventive Materials and Corrosion Testing, CRC Press, 2020, https://doi.org/10.1201/9781315101217.
[4] Y. Lyu, H. Ishida, Natural-sourced benzoxazine resins, homopolymers, blends and composites: A review of their synthesis, manufacturing and applications, Prog Polym Sci 99 (2019), https://doi.org/10.1016/j.progpolymsci.2019.101168.
[5] A. Hofland, Alkyd resins: From down and out to alive and kicking, Prog Org Coat 73 (2012) 274–282, https://doi.org/10.1016/j.porgcoat.2011.01.014.
[6] P.P. Chiplunkar, A.P. Pratap, Utilization of sunflower acid oil for synthesis of alkyd resin, Prog Org Coat 93 (2016) 61–67, https://doi.org/10.1016/j.porgcoat.2016.01.002.
[7] S. Vaithilingam, R. ThangavelRavivarman, A. Muthukaruppan, Development of cashew nut shell carbon reinforced thiourea based biophenolic benzoxazine-epoxy composites: High performance biobased coating materials, Polym Compos 41 (2020) 1950–1961, https://doi.org/10.1002/pc.25510.
[8] N. Kavitha, A. Chandramohan, K. Dinakaran, P. Prabukanthan, Recent developments in the polybenzoxazine based bionanocomposites: A review, Polym Adv Technol 35 (2024), https://doi.org/10.1002/pat.6466.
[9] Y. Zhang, X. Liu, G. Zhan, Q. Zhuang, R. Zhang, J. Qian, Study on the synergistic anticorrosion property of a fully bio-based polybenzoxazine copolymer resin, Eur Polym J 119 (2019) 477–486, https://doi.org/10.1016/j.eurpolymj.2019.07.020.
[10] K.I. Aly, M.G. Mohamed, O. Younis, M.H. Mahross, M. Abdel-Hakim, M.M. Sayed, Salicylaldehyde azine-functionalized polybenzoxazine: Synthesis, characterization, and its nanocomposites as coatings for inhibiting the mild steel corrosion, Prog Org Coat 138 (2020) 105385, https://doi.org/10.1016/j.porgcoat.2019.105385.
[11] H.A. Klfout, A.M. Asiri, K.A. Alamry, M.A. Hussein, Recent advances in bio-based polybenzoxazines as an interesting adhesive coating, RSC Adv 13 (2023) 19817–19835, https://doi.org/10.1039/d3ra03514j.

[12] Y. Gu, Q.-C. Ran, Polybenzoxazine/Fiber Composites. Handbook of Benzoxazine Resins, Elsevier, 2011, pp. 481–494, https://doi.org/10.1016/B978-0-444-53790-4.00073-4.
[13] S. Winroth, C. Scott, H. Ishida, Structure and performance of benzoxazine composites for space radiation shielding, Molecules 25 (2020), https://doi.org/10.3390/molecules25184346.
[14] B.-G. Sun, K.-X. Yang, Q. Lei, H.-Q. Shi, Y.-Q. Li, N. Hu, S.-Y. Fu, High residual mechanical properties at elevated temperatures of carbon fiber/acetylene-functional benzoxazine composite, Compos Part A Appl Sci Manuf 112 (2018) 11–17, https://doi.org/10.1016/j.compositesa.2018.05.021.
[15] C. Zhao, J. Wei, J. Wu, Y. Li, D. Xiang, Y. Wu, H. Li, Z. Hou, Synthesis and Characterization of Polyetheramine-type Benzoxazines as Protective Coatings for Low Carbon Steel against Corrosion in Sodium Chloride Solution, Int J Electrochem Sci 17 (2022), https://doi.org/10.20964/2022.06.43.
[16] Z. Hassan, Evalutating The Practicelevelof Universiy Governance Principlesat The University of Nawroz: An Academician's Perspective, The Journal of University of Duhok 25 (2022) 13–23, https://doi.org/10.26682/sjuod.2022.25.1.2.
[17] A. Sharma, G. Bhardwaj, H.S. Sohal, A. Gohain, Eugenol. Nutraceuticals and Health Care, Elsevier, 2022, pp. 177–198, https://doi.org/10.1016/B978-0-323-89779-2.00007-7.
[18] P. Madesh, H. Arumugam, B. Krishnasamy, A. Muthukaruppan, Synthesis of sustainable curcumin based photo-crosslinkable benzoxazines: Thermal, hydrophobic and anti-corrosion properties, J Mol Struct 1296 (2024), https://doi.org/10.1016/j.molstruc.2023.136902.
[19] Y. Deng, G.-L. Song, T. Zhang, Z. Lang, P. Wu, D. Zheng, Loading halloysite nanotubes on MXene as functional composite filler towards a polybenzoxazine anticorrosion coating, Colloids Surf A Physicochem Eng Asp 650 (2022) 129498, https://doi.org/10.1016/j.colsurfa.2022.129498.
[20] H.A. Klfout, A.M. Asiri, K.A. Alamry, M.A. Hussein, Recent advances in bio-based polybenzoxazines as an interesting adhesive coating, RSC Adv 13 (2023) 19817–19835, https://doi.org/10.1039/d3ra03514j.
[21] R. Malekkhouyan, M.G. Olivier, A review on the application of benzoxazine as coatings and corrosion inhibitors for corrosion protection of metallic substrates, Mater Today Chem 45 (2025), https://doi.org/10.1016/j.mtchem.2025.102614.
[22] A. Verma, N. Jain, R.R. Mishra, Applications and Drawbacks of Epoxy/Natural Fiber Composites. Handbook of Epoxy/Fiber Composites, Springer Singapore, Singapore, 2022, pp. 1–15, https://doi.org/10.1007/978-981-15-8141-0_32-1.
[23] H. Pulikkalparambil, S.M. Rangappa, S. Siengchin, J. Parameswaranpillai, Introduction to Epoxy Composites. Epoxy Composites, Wiley, 2021, pp. 1–21, https://doi.org/10.1002/9783527824083.ch1.
[24] Y. Bi, J. Li, J. Zhuang, P. Zhang, J. Yang, B. Liao, Q. Wang, W. Li, Unraveling the detrimental effect of polymeric microcapsules on the corrosion performance of epoxy resin coatings, Prog Org Coat 194 (2024), https://doi.org/10.1016/j.porgcoat.2024.108620.
[25] Y. Wang, B. Ou, P. Zhu, B. Niu, Y. Guo, Q. Zhi, High mechanical strength aluminum foam epoxy resin composite material with superhydrophobic, anticorrosive and wear-resistant surface, Surfaces and Interfaces 29 (2022), https://doi.org/10.1016/j.surfin.2022.101747.
[26] Y. Peng, B. Ou, Y. Peng, T. Cheng, M. Wen, H. Liu, Preparation of the fluorinated graphene/epoxy resin anti-corrosion composite coating, Diam Relat Mater (2024) 149, https://doi.org/10.1016/j.diamond.2024.111634.
[27] J. Jeong, Y. Ju, Y. Hong, D. Oh, M. Goh, Recyclable Curcumin-Based Bioepoxy Resin with On-Demand Chemical Cleavability, ACS Omega 9 (2024) 9585–9592, https://doi.org/10.1021/acsomega.3c09464.
[28] I. Abidli, N. Souissi, K. Essalah, X.R. Novoa, A combined experimental and theoretical approach effect of Curcuma. L extract as a corrosion inhibitor on iron in acidic solution, Canadian Metallurgical Quarterly 63 (2024) 793–811, https://doi.org/10.1080/00084433.2023.2240113.
[29] Q. Lan, X. Mao, C. Xia, D. Zhang, P. Huang, W. Zhang, S. Shi, Z. Wang, Curcumin based polyurethane materials and their functional applications: a review, Mater Res Express 11 (2024), https://doi.org/10.1088/2053-1591/ad48e1.
[30] J. Kerosenewala, P. Vaidya, V. Ozarkar, Y. Shirapure, A.P. More, Eugenol: extraction, properties and its applications on incorporation with polymers and resins—a review, Polymer Bulletin 80 (2023) 7047–7099, https://doi.org/10.1007/s00289-022-04414-9.
[31] A. Averick, S. Dolai, A. Punia, K. Punia, S.R. Guariglia, W. L'Amoreaux, K. Hong, K. Raja, Green anchors: Chelating properties of ATRP-click curcumin-polymer conjugates, React Funct Polym 102 (2016) 47–52, https://doi.org/10.1016/j.reactfunctpolym.2016.03.009.
[32] P.H.B.O. Nogueira, I.M. Costa, R.C.S. Araújo, V.M.D. Pasa, Bio-oil-based polyurethane coatings: A sustainable approach to corrosion protection, Prog Org Coat 194 (2024), https://doi.org/10.1016/j.porgcoat.2024.108572.
[33] G.K. Dutta, N. Karak, Bio-based waterborne polyester/cellulose nanofiber-reduced graphene oxide–zinc oxide nanocomposite: an approach towards sustainable mechanically robust anticorrosive coating, Cellulose 29 (2022) 1679–1703, https://doi.org/10.1007/s10570-021-04414-4.
[34] M.I Necolau, I.E. Bîru, J. Ghiţman, C. Stavarache, H. Iovu, Insightful characterization of sesamol-based polybenzoxazines: Effect of phenol and amine chain type on physical and nanomechanical properties, Polym Test 110 (2022) 107578, https://doi.org/10.1016/j.polymertesting.2022.107578.
[35] J. Dai, S. Yang, N. Teng, Y. Liu, X. Liu, J. Zhu, J. Zhao, Synthesis of eugenol-based silicon-containing benzoxazines and their applications as bio-based organic coatings, Coatings 8 (2018), https://doi.org/10.3390/coatings8030088.
[36] P. Thirukumaran, A. Shakila, S. Muthusamy, Synthesis and characterization of novel bio-based benzoxazines from eugenol, RSC Adv 4 (2014) 7959–7966, https://doi.org/10.1039/c3ra46582a.
[37] L. Dumas, L. Bonnaud, M. Olivier, M. Poorteman, P. Dubois, Eugenol-based benzoxazine: From straight synthesis to taming of the network properties, J Mater Chem A Mater 3 (2015) 6012–6018, https://doi.org/10.1039/c4ta06636g.
[38] C. Chen, Y. Cao, X. Lu, X. Li, H. Yao, Z. Xin, Copolymer of eugenol-based and pyrogallol-based benzoxazines: Low curing temperature and enhanced corrosion resistance, Colloids Surf A Physicochem Eng Asp 609 (2021), https://doi.org/10.1016/j.colsurfa.2020.125605.
[39] A. Hariharan, P. Prabunathan, A. Kumaravel, M. Manoj, M. Alagar, Bio-based polybenzoxazine composites for oil-water separation, sound absorption and corrosion resistance applications, Polym Test 86 (2020) 106443, https://doi.org/10.1016/j.polymertesting.2020.106443.
[40] Y. Zhang, X. Liu, G. Zhan, Q. Zhuang, R. Zhang, J. Qian, Study on the synergistic anticorrosion property of a fully bio-based polybenzoxazine copolymer resin, Eur Polym J 119 (2019) 477–486, https://doi.org/10.1016/j.eurpolymj.2019.07.020.
[41] Y. Zhang, X. Zhang, P. Wang, Y. Liu, M. Wan, K. Zhang, Phosphorus-free curcumin-derived epoxy resin with exceptional flame retardancy, glass transition temperature and mechanical properties, Polym Degrad Stab 215 (2023), https://doi.org/10.1016/j.polymdegradstab.2023.110440.
[42] J. Ramezanpour, B. Ramezanzadeh, N.A. Samani, Progress in bio-based anti-corrosion coatings; A concise overview of the advancements, constraints, and advantages, Prog Org Coat 194 (2024), https://doi.org/10.1016/j.porgcoat.2024.108556.
[43] A. Yadav, S. Panjikar, R.K. Singh Raman, Graphene-Based Impregnation into Polymeric Coating for Corrosion Resistance, Nanomaterials 15 (2025), https://doi.org/10.3390/nano15070486.
[44] M.Taufiq Musa, N. Shaari, S.K. Kamarudin, Carbon nanotube, graphene oxide and montmorillonite as conductive fillers in polymer electrolyte membrane for fuel cell: an overview, Int J Energy Res 45 (2021) 1309–1346, https://doi.org/10.1002/er.5874.
[45] B. Dey, M.W. Ahmad, A. ALMezeni, G. Sarkhel, D.S. Bag, A. Choudhury, Enhancing electrical, mechanical, and thermal properties of polybenzimidazole by 3D carbon nanotube@graphene oxide hybrid, Composites Communications 17 (2020) 87–96, https://doi.org/10.1016/j.coco.2019.11.012.
[46] M. Sabet, Advanced Functionalization Strategies for Carbon Nanotube Polymer Composites: Achieving Superior Dispersion and Compatibility, Polymer-Plastics Technology and Materials (2024), https://doi.org/10.1080/25740881.2024.2409312.
[47] Z. Baig, O. Mamat, M. Mustapha, Recent Progress on the Dispersion and the Strengthening Effect of Carbon Nanotubes and Graphene-Reinforced Metal Nanocomposites: A Review, Critical Reviews in Solid State and Materials Sciences 43 (2018) 1–46, https://doi.org/10.1080/10408436.2016.1243089.
[48] M. Matiyani, M. Pathak, B.S. Bohra, N.G. Sahoo, Noncovalent Functionalization of Carbon Nanotubes. Handbook of Carbon Nanotubes, Springer International Publishing, Cham, 2022, pp. 421–448, https://doi.org/10.1007/978-3-030-91346-5_66.
[49] J. Jeevanandam, A. Barhoum, Y.S. Chan, A. Dufresne, M.K. Danquah, Review on nanoparticles and nanostructured materials: history, sources, toxicity and regulations, Beilstein Journal of Nanotechnology 9 (2018) 1050–1074, https://doi.org/10.3762/bjnano.9.98.
[50] L. Zhang, H. Wu, Z. Zheng, H. He, M. Wei, X. Huang, Fabrication of graphene oxide/multi-walled carbon nanotube/urushiol formaldehyde polymer composite coatings and evaluation of their physico-mechanical properties and corrosion resistance, Prog Org Coat 127 (2019) 131–139, https://doi.org/10.1016/j.porgcoat.2018.10.026.
[51] J. Li, J. Cui, J. Yang, Y. Ma, H. Qiu, J. Yang, Silanized graphene oxide reinforced organofunctional silane composite coatings for corrosion protection, Prog Org Coat 99 (2016) 443–451, https://doi.org/10.1016/j.porgcoat.2016.07.008.
[52] P. Haghdadeh, M. Ghaffari, B. Ramezanzadeh, G. Bahlakeh, M.R. Saeb, The role of functionalized graphene oxide on the mechanical and anti-corrosion properties of polyurethane coating, J Taiwan Inst Chem Eng 86 (2018) 199–212, https://doi.org/10.1016/j.jtice.2018.02.009.
[53] M. Ramezanzadeh, B. Ramezanzadeh, M.G. Sari, M.R. Saeb, Corrosion resistance of epoxy coating on mild steel through polyamidoamine dendrimer-covalently functionalized graphene oxide nanosheets, Journal of Industrial and Engineering Chemistry 82 (2020) 290–302, https://doi.org/10.1016/j.jiec.2019.10.025.
[54] H. Wang, M. Ye, J. Wu, Y. Li, L. Guo, D. Yang, Development of amine functionalized graphene oxide/fluorinated polyurethane topcoat with integrated anti-corrosion, anti-aging, and anti-bacterial performance, Prog Org Coat 189 (2024) 108337, https://doi.org/10.1016/j.porgcoat.2024.108337.
[55] S. Krishnan, H. Arumugam, M. Chavali, A. Muthukaruppan, High dielectric, low curing with high thermally stable renewable eugenol-based polybenzoxazine matrices and nanocomposites, J Appl Polym Sci 136 (2019), https://doi.org/10.1002/app.47050.
[56] P. Paraskar, P. Bari, S. Mishra, Influence of amine functionalized graphene oxide on mechanical and thermal properties of epoxy matrix composites, Iranian Polymer Journal (English Edition) 29 (2020) 47–55, https://doi.org/10.1007/s13726-019-00772-w.
[57] H. Khani, O. Moradi, Influence of surface oxidation on the morphological and crystallographic structure of multi-walled carbon nanotubes via different oxidants. http://www.jnanochem.com/content/3/1/73, 2013.
[58] A. Aliyu, C. Srivastava, Correlation between growth texture, crystallite size, lattice strain and corrosion behavior of copper-carbon nanotube composite coatings, Surf Coat Technol 405 (2021), https://doi.org/10.1016/j.surfcoat.2020.126596.

[59] S.R. Nayak, K.N.S. Mohana, Corrosion protection performance of functionalized graphene oxide nanocomposite coating on mild steel, Surfaces and Interfaces 11 (2018) 63–73, https://doi.org/10.1016/j.surfin.2018.03.002.
[60] T. Riaz, R. Zeeshan, F. Zarif, K. Ilyas, N. Muhammad, S.Z. Safi, A. Rahim, S.A. A. Rizvi, I.U. Rehman, FTIR analysis of natural and synthetic collagen, Appl Spectrosc Rev 53 (2018) 703–746, https://doi.org/10.1080/05704928.2018.1426595.
[61] H.H. Khalil, M.M. El-Sheshtawy, S.N. Khattab, M.M. Abu-Serie, M.G. Shehat, M. Teleb, N.S. Haiba, Chemosensitization of non-small cell lung cancer to sorafenib via non-hydroxamate s-triazinedione-based MMP-9/10 inhibitors, Bioorg Chem 144 (2024), https://doi.org/10.1016/j.bioorg.2024.107155.
[62] J. Lalnunthari, Detection of Methyl tert-butyl Ether (MTBE) in Gasoline Fuel using FTIR: ATR spectroscopy, 2015. https://www.researchgate.net/publication/314154167.
[63] L. Hu, P. Jiang, P. Zhang, G. Bian, S. Sheng, M. Huang, Y. Bao, J. Xia, Amine-graphene oxide/waterborne polyurethane nanocomposites: effects of different amine modifiers on physical properties, J Mater Sci 51 (2016) 8296–8309, https://doi.org/10.1007/s10853-016-9993-5.
[64] M. Hassani, A. Tahghighi, M. Rohani, M. Hekmati, M. Ahmadian, H. Ahmadvand, Robust antibacterial activity of functionalized carbon nanotube- levofloxacine conjugate based on in vitro and in vivo studies, Sci Rep 12 (2022), https://doi.org/10.1038/s41598-022-14206-w.
[65] S. Arrechea, E.M.A. Guerrero-Gutiérrez, L. Velásquez, J. Cardona, R. Posadas, K. Callejas, S. Torres, R. Díaz, C. Barrientos, E. García, Effect of additions of multiwall carbon nanotubes (MWCNT, MWCNT-COOH and MWCNT-Thiazol) in mechanical compression properties of a cement-based material, Materialia (Oxf) 11 (2020), https://doi.org/10.1016/j.mtla.2020.100739.
[66] X. He, X. Xu, G. Bo, Y. Yan, Studies on the effects of different multiwalled carbon nanotube functionalization techniques on the properties of bio-based hybrid non-isocyanate polyurethane, RSC Adv 10 (2020) 2180–2190, https://doi.org/10.1039/c9ra08695a.
[67] S. Mohan, O.S. Oluwafemi, S.P. Songca, D. Rouxel, P. Miska, F.B. Lewu, N. Kalarikkal, S. Thomas, Completely green synthesis of silver nanoparticle decorated MWCNT and its antibacterial and catalytic properties. Pure and Applied Chemistry, Walter de Gruyter GmbH, 2016, pp. 71–81, https://doi.org/10.1515/pac-2015-0602.
[68] H. Diker, H. Bozkurt, C. Varlikli, Dispersion stability of amine modified graphene oxides and their utilization in solution processed blue OLED, Chemical Engineering Journal 381 (2020), https://doi.org/10.1016/j.cej.2019.122716.
[69] Z. Xu, T. Li, Z. Zhong, D. Zha, S. Wu, F. Liu, W. Xiao, X. Jiang, X. Zhang, J. Chen, Amide-linkage formed between ammonia plasma treated poly(<scp>D,L</scp>-lactide acid) scaffolds and bio-peptides: Enhancement of cell adhesion and osteogenic differentiation in vitro, Biopolymers 95 (2011) 682–694, https://doi.org/10.1002/bip.21635.
[70] T. Duguet, C. Bessaguet, M. Aufray, J. Esvan, C. Charvillat, C. Vahlas, C. Lacaze-Dufaure, Toward a computational and experimental model of a poly-epoxy surface, Appl Surf Sci 324 (2015) 605–611, https://doi.org/10.1016/j.apsusc.2014.10.096.
[71] S. Rani, M. Kumar, R. Kumar, D. Kumar, S. Sharma, G. Singh, Characterization and dispersibility of improved thermally stable amide functionalized graphene oxide, Mater Res Bull 60 (2014) 143–149, https://doi.org/10.1016/j.materresbull.2014.07.019.
[72] B.M. Sidi, M. Ben, B. Boussouari, M. Baitoul, Journal of Materials Science and Engineering with Advanced Technology A COMPARATIVE STUDY OF MULTI-WALLED CARBON NANOTUBES PURIFICATION TECHNIQUES A COMPARATIVE STUDY OF MULTI-WALLED CARBON NANOTUBES PURIFICATION TECHNIQUES. https://www.researchgate.net/publication/269222702, 2014.
[73] Y. Dessie, S. Tadesse, R. Eswaramoorthy, Surface Roughness and Electrochemical Performance Properties of Biosynthesized α-MnO2/NiO-Based Polyaniline Ternary Composites as Efficient Catalysts in Microbial Fuel Cells, J Nanomater 2021 (2021) 1–21, https://doi.org/10.1155/2021/7475902.
[74] L. Wu, Z. Zhou, K. Zhang, X. Zhang, G. Wang, Electrochemical and passive film evaluation on the corrosion resistance variation of Fe-based amorphous coating affected by high temperature, J Non Cryst Solids 597 (2022) 121892, https://doi.org/10.1016/j.jnoncrysol.2022.121892.
[75] J.R. Beryl, J.R. Xavier, Investigation of smart graphene oxide multilayer nanocoating for improved steel structural protection in natural seawater, J Mater Sci 59 (2024) 458–490, https://doi.org/10.1007/s10853-023-09190-z.
[76] N.A. Ismail, R.A. Shakoor, R. Kahraman, Corrosion inhibition performance of developed epoxy coatings containing carbon nanocapsules loaded with diethylenetriamine, Prog Org Coat 183 (2023) 107716, https://doi.org/10.1016/j.porgcoat.2023.107716.
[77] L.M. Muresan, Nanocomposite Coatings for Anti-Corrosion Properties of Metallic Substrates, Materials 16 (2023) 5092, https://doi.org/10.3390/ma16145092.
[78] J.R. Xavier, S.P. Vinodhini, J.Raja Beryl, Anti-corrosion and flame-retardant properties of environmentally benign smart functionalized WS2/rGO in epoxy coatings for enhanced steel structural protection in natural seawater, Mater Today Commun 38 (2024) 107842, https://doi.org/10.1016/j.mtcomm.2023.107842.
[79] N. Jeeva, K. Thirunavukkarasu, J.R. Xavier, Influence of multifunctional graphene oxide and silanized vanadium nitride in polyurethane coatings for the protection of aluminium alloy in aerospace industries, Diam Relat Mater 142 (2024), https://doi.org/10.1016/j.diamond.2024.110792.
[80] J. Gong, H. Wei, P. Hao, S. Li, X. Zhao, Y. Tang, Y. Zuo, Study on the Influence of Metal Substrates on Protective Performance of the Coating by EIS, Materials 17 (2024), https://doi.org/10.3390/ma17020378.
[81] B. Dou, H. Xiao, X. Lin, Y. Zhang, S. Zhao, S. Duan, X. Gao, Z. Fang, Investigation of the anti-corrosion properties of fluorinated graphene-modified waterborne epoxy coatings for carbon steel, Coatings 11 (2021) 1–16, https://doi.org/10.3390/coatings11020254.
[82] J.R. Xavier, S.P. Vinodhini, B. Ramesh, Optimizing aluminum alloy performance for marine superstructures: Advanced nanocomposite coating for enhanced corrosion resistance, flame retardancy, and mechanical strength, Polym Degrad Stab 227 (2024) 110847, https://doi.org/10.1016/j.polymdegradstab.2024.110847.
[83] J.R. Xavier, S.P. Vinodhini, R. Ganesan, Innovative nanocomposite coating for aluminum alloy: superior corrosion resistance, flame retardancy, and mechanical strength for aerospace applications, J Mater Sci 59 (2024) 12830–12861, https://doi.org/10.1007/s10853-024-09919-4.
[84] K.I. Aly, A. Mahdy, M.A. Hegazy, N.S. Al-Muaikel, S.-W. Kuo, M. Gamal Mohamed, Corrosion Resistance of Mild Steel Coated with Phthalimide-Functionalized Polybenzoxazines, Coatings 10 (2020) 1114, https://doi.org/10.3390/coatings10111114.
[85] S.R. Nayak, K.N.S. Mohana, M.B. Hegde, K. Rajitha, A.M. Madhusudhana, S. R. Naik, Functionalized multi-walled carbon nanotube/polyindole incorporated epoxy: An effective anti-corrosion coating material for mild steel, J Alloys Compd 856 (2021), https://doi.org/10.1016/j.jallcom.2020.158057.
[86] S.R. Nayak, K.N.S. Mohana, Corrosion protection performance of functionalized graphene oxide nanocomposite coating on mild steel, Surfaces and Interfaces 11 (2018) 63–73, https://doi.org/10.1016/j.surfin.2018.03.002.
[87] F. Zhang, W. Liu, L. Liang, M. Yang, S. Wang, H. Shi, Y. Xie, K. Pi, Application of polyether amine intercalated graphene oxide as filler for enhancing hydrophobicity, thermal stability, mechanical and anti-corrosion properties of waterborne polyurethane, Diam Relat Mater 109 (2020) 108077, https://doi.org/10.1016/j.diamond.2020.108077.
[88] R. Suleiman, H. Dafalla, B. El Ali, Novel hybrid epoxy silicone materials as efficient anticorrosive coatings for mild steel, RSC Adv 5 (2015) 39155–39167, https://doi.org/10.1039/C5RA04500B.
[89] Y. Ding, J. Zhong, P. Xie, J. Rong, H. Zhu, W. Zheng, J. Wang, F. Gao, L. Shen, H. He, Z. Cheng, Protection of Mild Steel by Waterborne Epoxy Coatings Incorporation of Polypyrrole Nanowires/Graphene Nanocomposites, Polymers (Basel) 11 (2019) 1998, https://doi.org/10.3390/polym11121998.
[90] Z. Zhou, C. Li, R. Wang, H. Tao, D. Yang, S. Qin, X. Meng, C. Zhou, Crosslinking control of hydrophobic benzoxazine-based hybrid sol-gel coating for corrosion protection on aluminum alloys, Prog Org Coat 171 (2022) 107059, https://doi.org/10.1016/j.porgcoat.2022.107059.
[91] C. Zhou, M. Tao, J. Liu, T. Liu, X. Lu, Z. Xin, Effects of Interfacial Interaction on Corrosion Resistance of Polybenzoxazine/SiO2Nanocomposite Coatings, ACS Appl Polym Mater 1 (2019) 381–391, https://doi.org/10.1021/acsapm.8b00114.
[92] Z. Zhou, J. Liu, X. Meng, C. Zhou, Improved corrosion resistance and hydrophobic stability of sol-gel coatings by benzoxazine modification on aluminum alloys AA1060, J Coat Technol Res 21 (1998), https://doi.org/10.1007/s11998.
[93] K. Rajitha, K.N.S. Mohana, S.R. Nayak, M.B. Hegde, A.M. Madhusudhana, An efficient and eco-friendly anti-corrosive system based on Beeswax- Graphene oxide nanocomposites on mild steel in saline medium, Surfaces and Interfaces 18 (2020), https://doi.org/10.1016/j.surfin.2019.100393.
[94] K. Rajitha, K.N. Mohana, Application of modified graphene oxide – Polycaprolactone nanocomposite coating for corrosion control of mild steel in saline medium, Mater Chem Phys 241 (2020), https://doi.org/10.1016/j.matchemphys.2019.122050.
[95] N. Muthukumar, H. Arumugam, B. Krishnasamy, M. Athianna, A. Muthukaruppan, Synthesis and Characterization of Sustainable Curcumin-Based Bio-benzoxazines for Antimicrobial and Anticorrosion Applications, ChemistrySelect 8 (2023), https://doi.org/10.1002/slct.202204302.
[96] H. Yang, Y. Liu, H. Chen, H. Li, Quaternary Ammonization Treatment Enhances the Antifouling Activities of Capsaicin-Based Polybenzoxazine Coatings, Langmuir 41 (2025) 5124–5135, https://doi.org/10.1021/acs.langmuir.4c04370.
[97] S.P. Vinodhini, J.R. Xavier, A. Priyadharshini, A review on flame retardant, anticorrosion, and mechanical properties of multifunctional polymer nanocomposite coatings for industrial applications, Prog Org Coat 206 (2025), https://doi.org/10.1016/j.porgcoat.2025.109361.
[98] J.R. Xavier, S.P. Vinodhini, A. Priyadharshini, Multifunctional epoxy-based nanocomposite coating for tinplate: Enhancing food packaging with superior mechanical, anticorrosion, and antimicrobial properties, Int J Biol Macromol 309 (2025), https://doi.org/10.1016/j.ijbiomac.2025.142671.
[99] J.R. Xavier, S.P. Vinodhini, J.Raja Beryl, Innovative multifunctional nanocomposite coated aluminum alloy for improved mechanical, flame retardant, and corrosion resistance in automobile industries, Journal of Adhesion (2024), https://doi.org/10.1080/00218464.2024.2378862.
[100] A. Trentin, R. Samiee, A.H. Pakseresht, A. Duran, Y. Castro, D. Galusek, Influence of pre-treatments on adhesion, barrier and mechanical properties of epoxy coatings: A comparison between steel, AA7075 and AA2024, Applied Surface Science Advances 18 (2023) 100479, https://doi.org/10.1016/j.apsadv.2023.100479.
[101] Y.M. Harsha, K.N.S. Mohana, M.C. Sunilkumar, M.C. Hithesh, M. Sreelakshmi, A. M. Madhusudhana, Syntheses of diphenolic resin based anti-corrosion coating material and reinforce its performance through MWCNT-Ag and MWCNT-Ag/

PANI nanofillers, Surf Coat Technol 485 (2024), https://doi.org/10.1016/j.surfcoat.2024.130871.
[102] I. Machado, I. Hsieh, E. Rachita, M.L. Salum, D. Iguchi, N. Pogharian, A. Pellot, P. Froimowicz, V. Calado, H. Ishida, A truly bio-based benzoxazine derived from three natural reactants obtained under environmentally friendly conditions and its polymer properties, Green Chemistry 23 (2021) 4051–4064, https://doi.org/10.1039/D1GC00951F.
[103] H. Yao, X. Lu, Z. Xin, X. Li, C. Chen, Y. Cao, Two novel eugenol-based difunctional benzoxazines: Synthesis and properties, Colloids Surf A Physicochem Eng Asp 616 (2021), https://doi.org/10.1016/j.colsurfa.2021.126209.
[104] B. Kiskan, Adapting benzoxazine chemistry for unconventional applications, React Funct Polym 129 (2018) 76–88, https://doi.org/10.1016/j.reactfunctpolym.2017.06.009.
[105] S. Tang, B. Lei, Z. Feng, H. Guo, P. Zhang, G. Meng, Progress in the Graphene Oxide-Based Composite Coatings for Anticorrosion of Metal Materials, Coatings 13 (2023), https://doi.org/10.3390/coatings13061120.
[106] Y. Zhu, S. Murali, W. Cai, X. Li, J.W. Suk, J.R. Potts, R.S. Ruoff, Graphene and Graphene Oxide: Synthesis, Properties, and Applications, Advanced Materials 22 (2010) 3906–3924, https://doi.org/10.1002/adma.201001068.
[107] Q. Zhang, G. Bai, W. Xiao, G. Sui, X. Yang, Effect of amine functionalized MWCNT-epoxy interfacial interaction on MWCNT dispersion and mechanical properties of epoxy-amine composites, Polym Compos 39 (2018), https://doi.org/10.1002/pc.24832.
[108] Q. Zhang, J. Wu, L. Gao, T. Liu, W. Zhong, G. Sui, G. Zheng, W. Fang, X. Yang, Dispersion stability of functionalized MWCNT in the epoxy–amine system and its effects on mechanical and interfacial properties of carbon fiber composites, Mater Des 94 (2016) 392–402, https://doi.org/10.1016/j.matdes.2016.01.062.
[109] M.C. Hithesh, K.N.S. Mohana, Y.M. Harsha, M. Sreelakshmi, A.M. Madhusudhana, M.C.S. Kumar, Effects of curing temperature and addition of functionalized graphene oxide on corrosion barrier performance of phenol furfural polymer-amino phenolic resin composite, Prog Org Coat 188 (2024), https://doi.org/10.1016/j.porgcoat.2023.108164.